



RESEARCH ARTICLE

Inhibition of the HEG1–KRIT1 interaction increases KLF4 and KLF2 expression in endothelial cells

Miguel Alejandro Lopez-Ramirez^{1,2} | Sara McCurdy¹ | Wenqing Li¹ | Mark K. Haynes³ | Preston Hale¹ | Karol Francisco^{4,5} | Killian Oukoloff⁵ | Matthew Bautista¹ | Chelsea H.J. Choi¹ | Hao Sun¹ | Brendan Gongol¹  | John Y. Shyy¹ | Carlo Ballatore⁵ | Larry A. Sklar³ | Alexandre R. Gingras¹ 

¹Department of Medicine, University of California San Diego, La Jolla, CA, USA

²Department of Pharmacology, University of California San Diego, La Jolla, CA, USA

³Department of Pathology, Center for Molecular Discovery, University of New Mexico School of Medicine, Albuquerque, NM, USA

⁴Department of Chemistry & Biochemistry, University of California San Diego, La Jolla, CA, USA

⁵Skaggs School of Pharmacy and Pharmaceutical Sciences, University of California San Diego, La Jolla, CA, USA

Correspondence

Alexandre R. Gingras, Department of Medicine, University of California San Diego, 9500 Gilman Drive, La Jolla, CA, USA.

Email: agingras@health.ucsd.edu

Funding information

DOE Office of Science User Facility, Grant/Award Number: DE-AC02-05CH11231; National Institutes of Health, Grant/Award Number: K01HL133530, P01HL151433-01 and NS092521; UCSD Academic Senate, Grant/Award Number: RS164R-GINGRAS; UC

ABSTRACT

The transmembrane protein heart of glass1 (HEG1) directly binds to and recruits Krev interaction trapped protein 1 (KRIT1) to endothelial junctions to form the HEG1–KRIT1 protein complex that establishes and maintains junctional integrity. Genetic inactivation or knockdown of endothelial HEG1 or KRIT1 leads to the upregulation of transcription factors Krüppel-like factors 4 and 2 (KLF4 and KLF2), which are implicated in endothelial vascular homeostasis; however, the effect of acute inhibition of the HEG1–KRIT1 interaction remains incompletely understood. Here, we report a high-throughput screening assay and molecular design of a small-molecule HEG1–KRIT1 inhibitor to uncover acute changes in signaling pathways downstream of the HEG1–KRIT1 protein complex disruption. The small-molecule HEG1–KRIT1 inhibitor 2 (HKi2) was demonstrated to be a bona fide inhibitor of the interaction between HEG1 and KRIT1 proteins, by competing orthosterically with HEG1 through covalent reversible interactions with the FERM (4.1, ezrin, radixin, and moesin) domain of KRIT1. The crystal structure of HKi2 bound to KRIT1 FERM revealed that it occupies the same binding pocket on KRIT1 as the HEG1 cytoplasmic tail. In human endothelial cells (ECs), acute inhibition of the HEG1–KRIT1 interaction by HKi2 increased KLF4 and KLF2 mRNA and protein levels, whereas a structurally similar inactive compound failed to do so. In zebrafish, HKi2 induced expression of *klf2a* in arterial and venous endothelium. Furthermore, genome-wide RNA transcriptome analysis of HKi2-treated ECs under static conditions revealed that, in addition to elevating KLF4 and KLF2 expression, inhibition of the HEG1–KRIT1 interaction mimics many of

Abbreviations: CXCR4, C-X-C chemokine receptor type 4; EC, endothelial cells; FERM, band 4.1, ezrin, radixin, and moesin; hCMEC/D3, human cerebral microvascular endothelial cell line; HEG1, heart of glass; HKi, HEG1–KRIT1 interaction inhibitor; HUVEC, human umbilical vein cells; KLF2, Krüppel-like Factor 2; KLF4, Krüppel-like Factor 4; KRIT1, Krev interaction trapped protein 1; LE, ligand efficiency; LLE, lipophilic ligand efficiency; MCP1, monocyte chemoattractant protein; MEKK3, MAPK/ERK kinase kinase 3; PARD3, partitioning defective 3 homolog; PI3K, phosphoinositide 3-kinase; SH2, Src homology 2; THBD, thrombomodulin; THBS1, thrombospondin 1.

Miguel Alejandro Lopez-Ramirez and Sara McCurdy Contributed equally.

This is an open access article under the terms of the Creative Commons Attribution-NonCommercial License, which permits use, distribution and reproduction in any medium, provided the original work is properly cited and is not used for commercial purposes.

© 2021 The Authors. *FASEB BioAdvances* published by the Federation of American Societies for Experimental Biology

Multi-campus Research Program, Grant/
Award Number: MRP-17-454909

the transcriptional effects of laminar blood flow. Furthermore, HKi2-treated ECs also triggered Akt signaling in a phosphoinositide 3-kinase (PI3K)-dependent manner, as blocking PI3K activity blunted the Akt phosphorylation induced by HKi2. Finally, using an in vitro colocalization assay, we show that HKi6, an improved derivative of HKi2 with higher affinity for KRIT1, significantly impedes recruitment of KRIT1 to mitochondria-localized HEG1 in CHO cells, indicating a direct inhibition of the HEG1–KRIT1 interaction. Thus, our results demonstrate that early events of the acute inhibition of HEG1–KRIT1 interaction with HKi small-molecule inhibitors lead to: (i) elevated *KLF4* and *KLF2* gene expression; and (ii) increased Akt phosphorylation. Thus, HKi's provide new pharmacologic tools to study acute inhibition of the HEG1–KRIT1 protein complex and may provide insights to dissect early signaling events that regulate vascular homeostasis.

KEYWORDS

endothelial cells, HEG1, KLF2, KLF4, KRIT1

1 | INTRODUCTION

The transmembrane protein heart of glass1 (HEG1) binds directly to and recruits Krev interaction trapped protein 1 (KRIT1) to endothelial cell (EC) junctions to regulate and maintain the organization of junctional molecules, which are critical for vertebrate cardiovascular development.^{1–4} We have solved the crystal structure of the HEG1–KRIT1 protein complex^{3,5} and found that the KRIT1 FERM domain binds to the HEG1 cytoplasmic tail C-terminus. These experiments revealed a new mode of FERM domain-membrane protein interaction. The KRIT1 FERM domain consists of three subdomains (F1, F2, and F3) forming a cloverleaf shape in which the F1 and F3 subdomain interface creates a hydrophobic groove that binds the Tyr^{1,380}-Phe^{1,381} of the most C-terminal portion of the HEG1 cytoplasmic tail.² Moreover, the KRIT1 FERM domain also simultaneously binds Rap1, a small GTPase, on the surface of the F1 and F2 subdomains, which acts to stabilize endothelial junctions through formation of the HEG1–KRIT1–Rap1 ternary complex.^{3,4,6} These studies suggest that part of the biological effects of KRIT1, related to endothelial junctional integrity, relies on the KRIT1 FERM domain being recruited to cell-cell junctions to interact with both HEG1 and Rap1.

HEG1 and KRIT1 are genetically linked in mice¹ and zebrafish during cardiovascular development.^{1,7,8} *Krit1*^{−/−} mice show gross defects in multiple vascular beds and early embryonic lethality.⁹ Similarly, *Heg1*^{−/−} mice result in lethal hemorrhage due to cardiovascular defects.¹ Studies in zebrafish embryos show that loss-of-function of *krit1* or *heg1* leads to vascular dilation and severe heart defects.^{1,10,11} It has been demonstrated that increases in endothelial Krüppel-like factors 4 and 2 (KLF4 and KLF2) may constitute a major

mechanism by which loss of HEG1 or KRIT1 alters cardiovascular development.^{12–16} Importantly, these changes in KLF4 and KLF2 were associated with increased MAPK/ERK kinase kinase 3 (MEKK3) activity in endothelial cells, which in turn, upregulates the MEK5-ERK5-MEF2 signaling axis.^{12–14,17} Paradoxically, the MEK5-ERK5-MEF2 mechanotransduction module regulates KLF4 and KLF2 expression during laminar blood flow^{18,19} to confer vascular integrity²⁰ and vasoprotection.²¹ A recent study by Donat et al. in zebrafish showed that *heg1* and *krit1* expression confer cardiovascular development accuracy by fine-tuning endothelial cell response to blood flow.⁷ The study reported that *heg1* expression is positively regulated by blood-flow, and stabilizes levels of *krit1* protein, thereby controlling expression of *klf2a/b*, a major mechanosensitive gene, in the zebrafish vasculature. Although genetic approaches have contributed enormously to our understanding of the fundamental molecular and cellular processes regulated by endothelial HEG1 and KRIT1 proteins, it remains unclear whether the effect of inhibiting HEG1–KRIT1 protein interaction in endothelial cells leads to similar outcomes such as those seen with loss of HEG1 or KRIT1 altogether.

Here, we performed a high-throughput screen followed by an exploration of the structure–activity relationship (SAR) of a new class of inhibitors of the HEG1–KRIT1 interaction to uncover acute changes in signaling pathways downstream of the HEG1–KRIT1 protein complex. Our findings indicate that HKi2 is a bona fide covalent reversible inhibitor by competing orthosterically with HEG1 for binding to the KRIT1 FERM domain. Our results further reveal that disruption of the HEG1–KRIT1 interaction by HKi2 triggers signaling pathways that have previously been associated with laminar blood flow, including: (i) an increase in KLF4 and KLF2 gene and protein

expression; and (ii) elevation of Akt signaling in the endothelium. As a result, HKi2 as well as other HKi derivatives hold promise as new tools to study acute disruption of endothelial HEG1–KRIT1 binding, and may provide insights to dissect the pathways regulated by the HEG1–KRIT1 protein complex to control early signaling events regulating vascular homeostasis.

2 | MATERIAL AND METHODS

2.1 | Material

All reagents were from Sigma unless otherwise indicated. Plasticware was from VWR and Greiner Bio-One. Neutravidin Bead sets for were from SpheroTech, Inc. All solutions were prepared with ultrapure 18 MΩ water or anhydrous DMSO. Flow cytometric calibration beads were from Bangs Laboratories Inc., and SpheroTech, Inc. Off-patent commercial libraries were purchased from Prestwick Chemical, SelleckChem, Spectrum Chemical, and Tocris Bio-Science. We also purchased a collection of on-patent drugs from MedChem Express that was specifically assembled by UNM collaborators. All purchased libraries were provided as 10 mM stock solutions in 96-well matrix plates except the MedChem Express library which was provided as individual powders that were subsequently solubilized in DMSO. All libraries were reformatted using a Biomek FX^P laboratory automated workstation into 384-well plates for storage (Greiner #784201; Labcyte #PP-0200). Low-volume dispensing plates (Labcyte #LP-0200) were assembled using an Agilent BioCell workstation (Santa Clara, CA). The following compounds were purchased from: Sirtinol (Selleckchem); 2-hydroxy-1-naphthaldehyde (Ark Pharm); and 2-amino-*N*-(1-phenylethyl) benzamide (Enamine).

2.2 | Plasmid construction and protein purification

HEG1 intracellular tail model protein was prepared as previously described.⁵ In brief, His6-tagged HEG1 intracellular tail containing an *in vivo* biotinylation peptide tag at the N-terminus was cloned into pET15b, expressed in BL21 Star (DE3) and purified by nickel-affinity chromatography under denaturing conditions. Synthetic human non-biotinylated HEG1 7-mer peptide (residues 1375–1381) was purchased from GenScript.

His6-EGFP-KRIT1 (WT) FERM domain (417–736) and KRIT1(L717,721A) mutant were cloned into pETM-11 and expressed in BL21 Star (DE3). Recombinant His-EGFP-KRIT1 was purified by nickel-affinity chromatography, and further purified by Superdex-75 (26/600) size-exclusion chromatography (GE Healthcare). The protein concentration was assessed using the A280 extinction coefficient of 71,740 M⁻¹.

Human KRIT1 FERM domain, residues 417–736 was expressed and purified as described previously.³ Briefly, KRIT1 was cloned into the expression vector pLEICS-07 and expressed in *Escherichia coli* BL21 Star (DE3) (Invitrogen). Recombinant His-tagged KRIT1 was purified by nickel-affinity chromatography; the His tag was removed by cleavage with tobacco etch virus protease overnight, and the protein was further purified by Superdex-75 (26/600) size-exclusion chromatography. The protein concentration was assessed using the A280 extinction coefficient of 45,090 M⁻¹.

Human Rap1 isoform Rap1b (residues 1–167) cloned into pTAC vector in the *E. coli* strain CK600K was the generous gift of Professor Alfred Wittinghofer (Max Planck Institute of Molecular Physiology). The Rap1b was expressed and purified as described previously.²² The protein concentration was assessed using a molar absorption coefficient of A280 = 19,480 M⁻¹ as previously reported.²³

Equimolar concentrations of KRIT1 FERM domain and GMP-PNP loaded Rap1b were mixed and loaded on a Superdex-75 (26/600). The column was pre-equilibrated and run with 20 mM Tris, 50 mM NaCl, 3 mM MgCl₂, and 2 mM DTT (pH 8). The final complex concentration was determined using a molar absorption coefficient of A280 = 61,310 M⁻¹ for the KRIT1-Rap1b complex.

2.3 | Bead coupling

SPHERO Neutravidin Polystyrene Particles, 6–8 μM (SpheroTech) were washed twice with wash buffer (20 mM Tris, 150 mM NaCl, pH 7.4 containing 0.01% NP-40, and 1mM EDTA). Prior to incubation with biotin-tagged HEG1 cytoplasmic tail protein, an appropriate volume of bead slurry was passivated to inhibit nonspecific binding by incubation for 30 min at room temperature in reaction buffer containing 0.1% BSA (20 mM Tris, 150 mM NaCl, pH 7.4 0.01% NP-40, 1mM EDTA, 1mM DTT, and 0.1% BSA). Passivated beads were collected by centrifugation, resuspended to 3,600 particles/μL in reaction buffer and biotinylated HEG1 tail was added to a final concentration of 150 nM, and incubated overnight on a rotator at 4°C. The beads were washed three times by centrifugation with ice-cold reaction buffer to remove unbound HEG1 peptide. Beads were diluted such that a final concentration of 2000 beads/μL was available for addition to assay plates.

2.4 | Flow cytometry assay

A final volume of 100 μL containing 140 nM EGFP-KRIT1 FERM domain, with 10% DMSO or 10% compounds in DMSO, was incubated for 15 min at room temperature on a rotator. 100 μL of beads were added to the mixture for a final

volume of 200 μL at 1000 particles/ μL with 70 nM EGFP-KRIT1 and incubated for 15 min at room temperature on a rotator. The control beads were: without KRIT1 (minimum signal); with KRIT1 (maximum signal); and with KRIT1 plus 2 μM HEG1 7-mer (positive blocking control). The EGFP fluorescence was measured using a BD Accuri flow cytometer. For screening purposes, the final volume of the reaction was scaled down to 10 μL and samples were processed as previously described.²⁴ For Figures 1D–F, 2B, and 3E, a representative experiment is shown of at the least 3 independent repeats.

2.5 | Assay plate assembly

Plate assays were performed in 384-well microtiter plates (Greiner Bio-one, #784101). Reaction buffer, HEG1-coupled beads, and EGFP-KRIT-FERM constructs were added using a MultiFloTM Microplate Dispenser (BioTek Instruments, Inc.). Compounds were added to single-point assay plates pre-loaded with reaction buffer using a Biomek^{NX} liquid handler (BeckmanCoulter) equipped with a 100 nL pintool (V & P Scientific, Inc.). Compound libraries were dispensed to a final concentration of 10 μM . An equal volume (10 nL) of DMSO was added to the vehicle control wells. Following the addition of library compounds, 5 μL of assay buffer was added and the plates were mixed before addition of 5 μL of the protein-coupled bead mixtures; Plates were protected from light and incubated on a rotator for 15 min at room temperature. Binding of EGFP-KRIT to HEG1 coupled beads was evaluated using an Accuri C6 flow cytometer.

Dose–response plates were assembled similarly. In this instance, test compounds were added to dose response plates using a dilution protocol of the acoustic dispenser that resulted in a final concentration range of 100–0.015 μM .

2.6 | Data acquisition

Assay plates were sampled using the HyperCytTM high throughput flow cytometry platform (Intellicyt). During sampling, the probe moves from well to well and samples 1–2 μL from each well pausing 0.4 s in the air before sampling the next well. The resulting sample stream consisting of 384 separated samples is delivered to an Accuri C6 flow cytometer (BD Biosciences). Plate data are acquired as time-resolved files that are parsed by software-based well identification algorithms and merged with compound library files. Plate performance was validated using the Z-prime calculation.²⁵

Compounds that satisfied hit selection criteria in the primary screen were cherry-picked from compound storage plates and tested to confirm activity and determine potency. Dose–response data points were fitted by Prism software

(GraphPad Software Inc.) using nonlinear least-squares regression in a sigmoidal dose–response model with variable slope, also known as the 4-parameter logistic equation. Curve fit statistics were used to determine the concentration of test compound that resulted in 50% of the maximal effect (EC_{50}), the confidence interval of the EC_{50} estimate, the Hill slope, and the curve fit correlation coefficient.

2.7 | Crystallization of the KRIT1-Rap1b-HKi complexes

The purified KRIT1 FERM domain-Rap1b complex at 8.25 mg/mL was used for crystallization. Crystals were grown at room temperature using the sitting-drop method by mixing equal volumes of protein complex and reservoir solution (2 + 2 μL). The reservoir solution contained 20–25% PEG 3350, 100 mM Tris, pH 8.5, 100 mM KCl. After 1 week or later, ~0.5 μL of 10 mM HKi compounds in DMSO was added to the drop for 1 day. The crystals were briefly transferred to the reservoir solution containing 20% glycerol before freezing in liquid nitrogen.

2.8 | Structure determination

Diffraction data for the KRIT1 FERM domain-Rap1b-HKi complexes were collected at the Advanced Light Source beamline 5.0.3. The data were processed with XDS.²⁶ The structures were solved by molecular replacement using Phaser with the structure of the KRIT1-Rap1b complex (PDB ID: 4hdo). The model was then optimized using cycles of manual refinement with Coot and maximum likelihood refinement in Refmac5 as part of the CCP4 software suite.²⁷ The small-molecule inhibitors (HKi1 and HKi2) were built using Coot Ligand Builder.

2.9 | PARD3 pulldown assay

Neutravidin agarose beads (Thermo Fisher) matrix with HEG1 wild-type cytoplasmic tail (1274–1381) or HEG1 ΔYF cytoplasmic tail (1274–1379) were prepared as previously described.^{5,28} HUVEC were collected in cold lysis buffer (50 mM Tris-HCl, pH 7.4, 100 mM NaCl, 5 mM MgCl_2 , 0.5% NP-40) plus protease inhibitor cocktail (Roche). A total of 20 μL of HEG1 matrix was added to 600 μg of clarified lysates and incubated at 4°C overnight while rotating. All conditions contained either vehicle DMSO, 35 μM HKi2, or 35 μM 2-hydroxy-1-naphthoic acid. After three washes with cold lysis buffer, beads were mixed with sample buffer and proteins were separated by SDS–PAGE. Bound PARD3 was detected by using polyclonal rabbit anti-PARD3 (Millipore, 07-330) antibody.

2.10 | Identification of covalent reversible binding by Schiff base

Recombinant KRIT1 FERM domain at 1 mg/mL (26.8 μ M) in 100 μ L PBS was incubated with either vehicle control (DMSO) or HKi2 (50 μ M) for 15 min at room temperature. A 10-fold excess of sodium borohydride (500 μ M) was added and the reaction incubated overnight. The samples were denatured by adding 5x sample buffer and a total of 10 μ g of protein was subjected to SDS-PAGE per sample. The gel was stained with Coomassie, then the bands were excised and sent for protein analysis by in-gel trypsin digest followed by liquid chromatography (LC) in combination with tandem mass spectroscopy (MS/MS) using electrospray ionization or LC-MS/MS analysis, (see supplementary methods). Protein identification and label free quantification was carried out using Peaks Studio 8.5 (Bioinformatics solutions Inc.). The searches in Peaks used mass of 157.0653 in (monoisotopic mass) to lysine residues as variable modification. Searches for this mass shift identified Lys⁷²⁰ as forming a covalent bond with HKi2.

2.11 | Cell culture

hCMEC/D3 (human cerebral microvascular endothelial cell line) cells used from passages 30 to 37 after they were grown to confluence on collagen-coated plates as previously described.²⁹ Cells were cultured in EGM-2 MV medium, with all supplements added as directed by the manufacturer (Lonza). HUVEC (Human Umbilical Vein Cells, Lonza), used from passages 4 to 7, were grown to confluence on fibronectin-coated plates, and maintained using complete EGM-2 media (Lonza). HKi2, 10 mM in DMSO, was maintained at room temperature for 30 min rotating before use. Cells were then treated with HKi2 at the concentrations and times indicated for each experiment. Treatments with 50 or 75 μ M HKi2 were doses selected for maximal effects on hCMEC/D3 and HUVECs, respectively (Figures 6 and 7). Vehicle control cells were treated with the same concentration of DMSO. Cells were maintained at 37°C in 5% CO₂. Chinese hamster ovary (CHO) cells were grown on glass coverslips and maintained in DMEM supplemented with 10% FBS, 1% penicillin/streptomycin, and 1% L-glutamine. CHO cells were co-transfected with EGFP-KRIT1 FERM domain, and either mito-mCherry-HEG1 or HEG1 Δ YF cytoplasmic tail expression plasmids. Mito-mCherry-HEG1 wild-type or Δ YF were cloned into pcDNA3.1(-) as previously reported.²⁸ Human KRIT1 cDNA encoding EGFP-tagged KRIT1 FERM domain was previously described.⁴

2.12 | Propidium Iodide Staining

Following stimulation with 50 μ M HKi2, inactive compound (compound 9), or vehicle control (DMSO) for 24 h, hCMEC/

D3 monolayers were washed twice with HBSS (no CaCl₂, MgCl₂, MgSO₄) and detached by 0.25% trypsin/EDTA. The cells were resuspended in PBS with 1% BSA and stained with propidium iodide (PI, BD Pharmingen). The cell viability was assessed by flow cytometry using a BD Accuri 6+ machine, with PI-positive cells considered dead.

2.13 | Immunofluorescence

hCMEC/D3 cells were grown to confluence on collagen-coated glass coverslips, and cells were treated with 50 μ M HKi2 or inactive compound (2-hydroxy-1-naphthoic acid, compound 9) for 12 h. Cells were washed two times with PBS, then fixed for 10 min at room temperature with 4% PFA in PBS, pH 7.4, and permeabilized with 0.5% Triton X-100 in PBS for 5 min. The slides were blocked with 0.5% BSA in PBS for 30 min and incubated with goat polyclonal antibody anti-KLF4 (1:100; AF3640; R&D Systems) overnight at room temperature. Cells were washed four times with PBS and incubated for 1 h at room temperature with a donkey anti-goat Alexa Fluor-488 coupled secondary antibody (1:300; Jackson Lab; 705-546-147) in PBS. Cell nuclei were stained with DAPI and mounted with Fluoromount-G mounting medium (SouthernBiotech).

2.14 | Western blotting and immuno precipitation

Following stimulation with 50 μ M HKi2 or vehicle control (DMSO) for 1 h, hCMEC/D3 cells were rapidly washed twice with ice cold HBSS (with CaCl₂, MgCl₂, MgSO₄) and lysed with RIPA buffer (50 mM Tris, pH 7.5, 150 mM NaCl, 1% NP-40, 0.5% Sodium Deoxycholate, 0.1% SDS, 2 mM EDTA, and 50 mM NaF) containing 2.5X protease inhibitor cocktail, 2.5x PhosSTOP, and 1 mM Na₃VO₄). Cell lysates were spun at 20,000xg for 15 min at 4°C and the supernatants resuspended in 1X SDS sample buffer. Samples were resolved on 4%–12% gradient gel and blotted using specific antibodies, as indicated. Antibodies to phospho-Akt-Ser473 (clone: 193H12; rabbit mAb; #4058; 1:250), and total Akt (clone: 40D4; mouse mAb; #2920; 1:500) were purchased from Cell Signaling Technology. Band intensity was determined using a Li-Cor near infrared scanner, and values obtained for phosphoproteins were normalized to the total protein in the same sample.

2.15 | RNA extraction and qRT-PCR

For RNA-Seq: HUVECs total RNA was isolated using a MagMAX™-96 for Microarrays Total RNA Isolation Kit,

according to the manufacturer's protocol (Thermo Fisher Scientific Cat# AM1839). qPCR analysis, single-stranded cDNA was produced from 10 ng RNA isolated from HUVECs and hCMC/D3 using PrimeScript™ RT Master Mix according to the manufacturer's protocol (Takara Cat. #RR036A). The levels of genes were analyzed using iTaq™ Universal SYBR Green (BioRad Cat# 1725122) and thermal cycler (CFX96 Real-Time System; Bio-Rad) according to the manufacturer's protocol. Actin mRNA levels was used as internal control, and the $2^{-\Delta\Delta CT}$ method was used for data analysis.

For qPCR: HUVECs and hCMC/D3 cells total RNA was isolated using TRIzol reagent, according to the manufacturer's protocol (Thermo Fisher Scientific). Single-stranded cDNA was produced from 1 µg RNA isolated from HUVECs and hCMC/D3 using SuperScript III Reverse Transcriptase according to the manufacturer's protocol (Invitrogen). KAPA SYBR FAST qPCR Master Mix (KAPA BIOSYSTEMS) was used to determine the relative levels of human genes using the following primer sets: *KLF2*, (forward) AGACCACGATCCTCCTTGA and (reverse) TCACAAGCCTCGATCCTCTA; *KLF4*, (forward) GGTCTGTGACTGGATCTTCTATC and (reverse) ACCCTGATATCCACAACCTTC; *VEGFa*, (forward) GCTTACTCTCACCTGCTTCTG and (reverse) CTGTCATGGGCTGCTTCTT; *THBS1*, (forward) AAGCACACGCAACTCTCA and (reverse) CTCCTCCCTCATCCACATTTAC; *THBD*, (forward) CCCAGGAGACAGTTCAAGAAAG and (reverse) CCCAATTCACACAAGACCAGTAG; *MCPI* (*CCL2*), (forward) TCATAGCAGCCACCTTCATTC and (reverse) CTCTGCACTGAGATCTTCCTATTG, with *ACTB* (forward) GGACCTGACTGACTACCTCAT and (reverse) CGTAGCACAGCTTCTCCTTAAT (reverse) used as internal control. The $2^{-\Delta\Delta CT}$ method was used for data analysis and each condition was considered independent and compared with their respective control.

2.16 | Genome-wide RNA sequencing

The RNA was first analyzed for quantity (ND-1000 spectrophotometer; NanoDrop Technologies) and quality (Bioanalyzer; Agilent). Only RNA with a RNA integrity number (RIN) greater than 8 was used for library preparation. Libraries were generated using Illumina's TruSeq Stranded mRNA Sample Prep kit using 400 ng RNA. RNA libraries were multiplexed and sequenced with 100-bp paired single-end reads (SR100) to a depth of 30 million reads per sample on an Illumina HiSeq2500. Fastq files from RNA-seq experiments were mapped to the human genome (GRCh primary assembly release 96) using Hisat2 with default parameters. All bioinformatics analyses were conducted in R using the systempipeR package RNAseq workflows. Differential gene expression analysis was conducted with EdgeR.

2.17 | Zebrafish

A previously reported transgenic zebrafish line *Tg(klf2a:H2B-EGFP)* combined with *Tg(kdrl:mCherry)* was used to monitor the expression of *klf2a* in endothelial cells.^{30,31} They embryos were treated at 26 h post-fertilization (hpf) with HKi2 (4 µM), inactive compound (4 µM) (compound 9), or vehicle (DMSO) for 4 h. We found the compounds to be well tolerated and soluble in fish egg water. At 30 hpf, these embryos were paralyzed with tricaine (Sigma A-5040) for confocal imaging and analyzed for EGFP and mCherry expression using a Zeiss LSM 880 Airiscan microscope. The intensity of nuclear EGFP within the vasculature of zebrafish embryos was quantified by ImageJ. Each nucleus was outlined on XY planes continually through Z axis for the measurement. Intensity of seven nuclei was measured from each embryo. Two HKi2 treated embryos and two control embryos were measured from one experiment, and results from two independent experiments were analyzed.

2.18 | Statistical analyses

For qPCR and western blots, the data were expressed as means ± standard error of the mean (SEM). For all experiments, the number of independent experiments (n) is indicated. A two-tailed Student's *t*-test was used to determine statistical significance. For comparisons with more than two groups, one-way ANOVA was used.

GraphPad Prism 5 software was used for data analysis of the beads assay. We used the one-site total binding equation to generate the EC₅₀ and IC₅₀ (Figures 1E,F, 2B, 3E and 5B).

3 | RESULTS

3.1 | A flow cytometry assay to study HEG1–KRIT1 protein interaction

We previously solved the crystal structure of the KRIT1 FERM domain bound to the C-terminal region of the HEG1 cytoplasmic tail (Figure 1A).⁵ Because the HEG1 binding pocket on the KRIT1 FERM domain is both discrete and unique, we hypothesized that specific inhibitors of the HEG1–KRIT1 protein complex could be identified. To test this hypothesis, we developed a high-throughput flow cytometry-screening assay to identify compounds that block the HEG1–KRIT1 protein-protein interaction. We had previously shown that the HEG1 cytoplasmic tail can be used as an affinity matrix for KRIT1 binding⁵ and this matrix was also used to identify HEG1 interactions with other proteins, such as Rasip1.²⁸ Using a similar approach, we coupled the biotinylated HEG1 cytoplasmic tail (a.a. 1274–1381) peptide to 6-micron SPHERO Neutravidin-coated beads (Figure 1B). We first added varying amounts of biotinylated HEG1 peptide

to the beads (Figure 1C). The addition of purified recombinant GFP-KRIT1 FERM domain to the HEG1 matrix beads, without washes, leads to a dose-dependent GFP intensity increase by flow cytometry (Figure 1D). Importantly, we observed many beads forming doublets at a 1500 nM HEG1 concentration in the light scatter signals, which affected the GFP signal (Figure 1C). Therefore, we used a concentration of 150 nM biotinylated HEG1 for the assay, which gave the best signal without aggregation of the beads. Second, the addition of increasing amounts of purified recombinant GFP-KRIT1 FERM domain to the HEG1 matrix

beads, without washes, lead to a dose-dependent GFP intensity increase by flow cytometry with $EC_{50} = 32.4$ nM (Figure 1E, blue line), showing that GFP-KRIT1 binds the HEG1 tail on the beads. Importantly, a KRIT1 (L717,721A) mutant previously shown to have significantly reduced affinity for HEG1,⁵ revealed a dramatic reduction in binding to HEG1 using our bead assay (Figure 1E, red line), validating this approach and confirming specific binding. Additionally, incubation of the GFP-KRIT1 FERM domain with a non-biotinylated HEG1 C-terminus 7-mer peptide blocked the interaction in a dose-dependent manner with $IC_{50} = 410$ nM

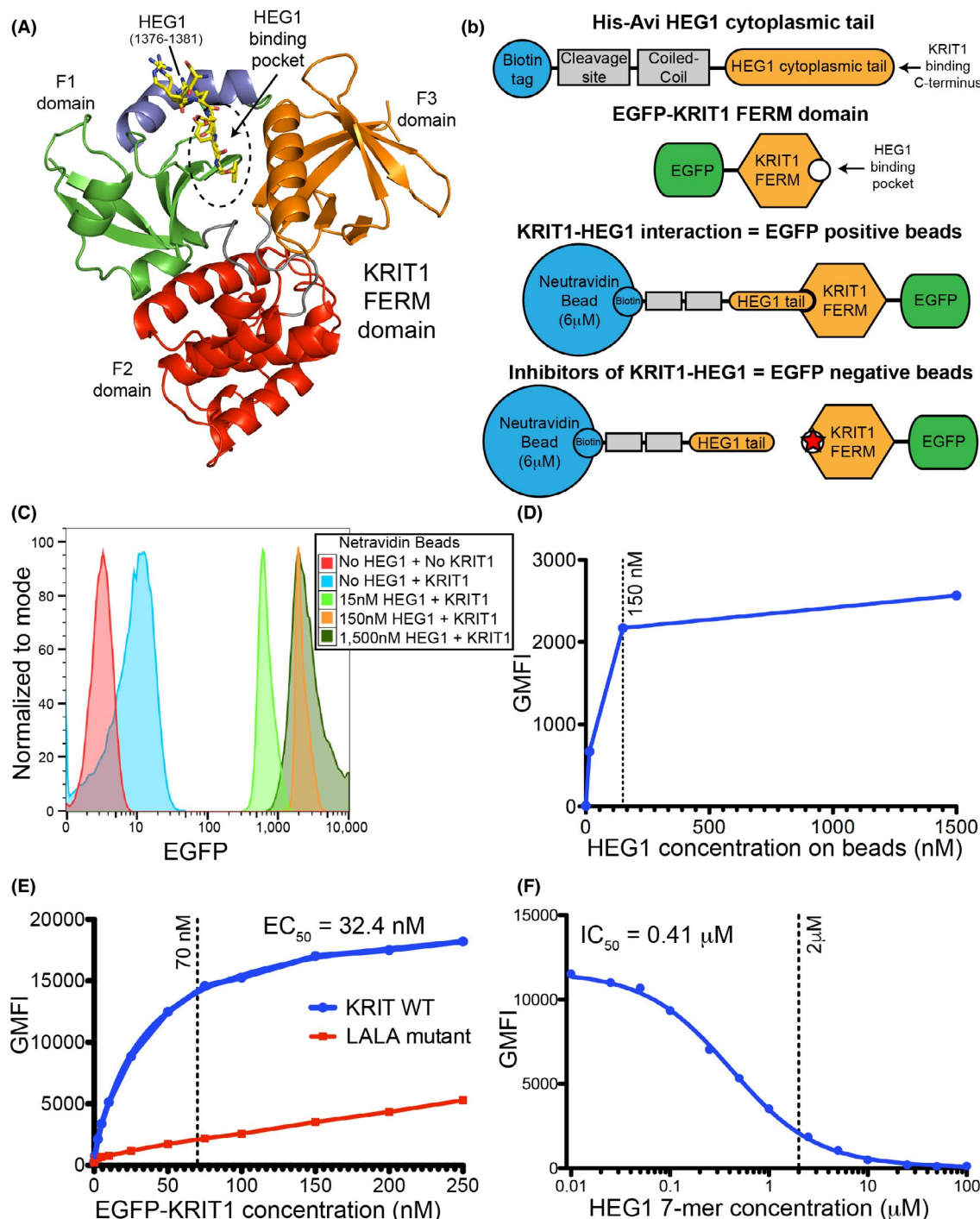


FIGURE 1 Flow cytometry assay for the HEG1–KRIT1 FERM domain interaction. (A) Ribbon diagram of KRIT1 FERM domain in complex with the HEG1 cytoplasmic tail (PDB ID: 3u7d). The HEG1 peptide is shown in yellow. The KRIT1 FERM domain consists of three subdomains: F1 (green and blue); F2 (red); and F3 (orange). The feature of the F1 domain that is not present in other FERM domain is shown in blue and that region is an important part of the HEG1 binding pocket. (B) Schematic representation of the HEG1 cytoplasmic tail (a.a. 1274–1381) peptide coupled to Neutravidin beads and the EGFP-KRIT1 FERM domain. Binding of EGFP-KRIT1 FERM domain to the HEG1 matrix beads can be detected by flow cytometry. Small-molecule inhibitors HKi preventing the interaction of EGFP-KRIT1 FERM domain with the HEG1 matrix beads reduce the EGFP fluorescence signal. (C) Flow cytometry profile of SPHERO Neutravidin Polystyrene Particles coated with increasing amount of biotinylated HEG1 peptide and 150 nM EGFP-KRIT1 FERM domain. We noticed many beads doublets in the light scatter signal at 1,500 nM concentration of HEG1 peptide. (D) Titration curve for the interaction of EGFP-KRIT1 FERM domain with increasing amounts of HEG1 on the beads as shown in panel C, as measured by geometric mean fluorescence intensity (GMFI). We used the 150 nM HEG1 peptide concentration for future experiments. (E) Titration curve for the interaction of 150 nM HEG1 on the beads with increasing amounts of EGFP-KRIT1 FERM domain (0–250 nM) wild-type (blue line) and KRIT1(L717,721A) mutant (red line). We used the 70 nM EGFP-KRIT1 concentration for future experiments. (F) Competition binding curve of 70 nM EGFP-KRIT1 FERM domain binding to 150 nM HEG1 on the beads with increasing amounts on non-biotinylated HEG1 7-mer peptide. We used the 2 μ M HEG1 7-mer concentration for future experiments.

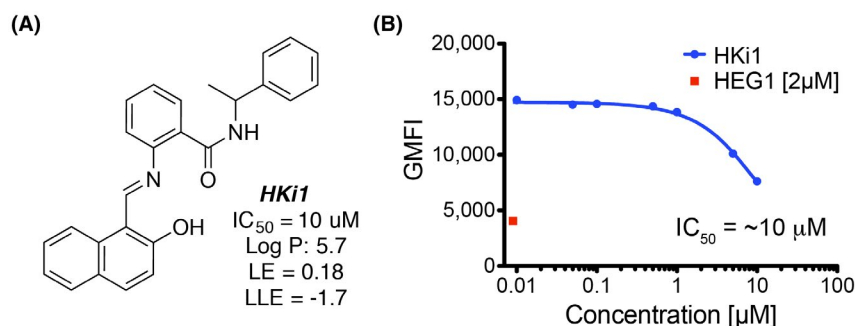


FIGURE 2 HKi1 is an inhibitor of the HEG1–KRIT1 interaction. (A) Chemical structure of HKi1. $LE = (1.37/HA) \times pIC_{50}$ where HA is the number of non H atoms present in the ligand; $LLE = pIC_{50} - \log P$. (B) Competition binding curve of 70 nM EGFP-KRIT1 FERM domain binding to 150 nM HEG1 on the beads with increasing amounts of HKi1. HKi1 had poor solubility in our buffer and concentrations $>30 \mu M$ could not be reached.

(Figure 1F). These results reveal a reliable and quantitative assay to study the HEG1–KRIT1 protein interaction by flow cytometry.

3.2 | High-throughput screening identifies inhibitors of HEG1–KRIT1 protein interaction

In order to screen a large number of compounds with potential to block the interaction between KRIT1 and HEG1, the flow cytometry assay was miniaturized for high throughput in a 384-well plate format. The assay required only 10 μL of sample per well in nanomolar concentrations with a count of 1000 beads per μL . We performed a pilot screen using an automated sample loader attached to a flow cytometer and analyzed 2 μL of sample per well (2000 beads). By alternating beads with GFP-KRIT1 in the absence or presence of 2 μM HEG1 7-mer blocking peptide (Figure S1A,B), we measured a Z' of 0.528 (Table S1).²⁵ Out of 6026 compounds screened we identified four confirmed hits (Table S1). Among these, the HEG1–KRIT1 inhibitor 1 (HKi1) (Figure 2A), exhibited promising activity in the assay with an IC_{50} value of $\sim 10 \mu M$ (Figure 2B). However, consistent with a high $\log P$ value of 5.7, HKi1 had limited aqueous solubility at 50 μM

concentrations or higher in our buffer conditions. As a result, saturated conditions in the assay could not be achieved.

3.3 | Crystal structure of KRIT1 FERM domain in complex with HKi1

Since we previously determined two crystal structures of the KRIT1 FERM domain bound to a HEG1 peptide^{3,5} (Figure 1A), we then crystallized the KRIT1 FERM domain in the presence of HKi1 and solved the structure of the complex to 1.75 Å resolution (Figure 3A and Table 1). The structure confirmed that this compound occupies the same pocket as the HEG1 (Figure 3B), supporting that HKi1 blocks the interaction by competing orthosterically with the HEG1 for binding to KRIT1 FERM domain. HKi1 is mostly hydrophobic ($\log P = 5.7$), as the HEG1 C-terminal Tyr-Phe residues, and sits in the hydrophobic pocket formed at the interface of the F1 and F3 subdomains of the KRIT1 FERM domain. Interestingly, good electron density was observed for approximately half of the molecule, and less well-defined electron density was observed for the other half of the molecule (Figure 3D), suggesting that modifications to HKi1 could improve binding properties.

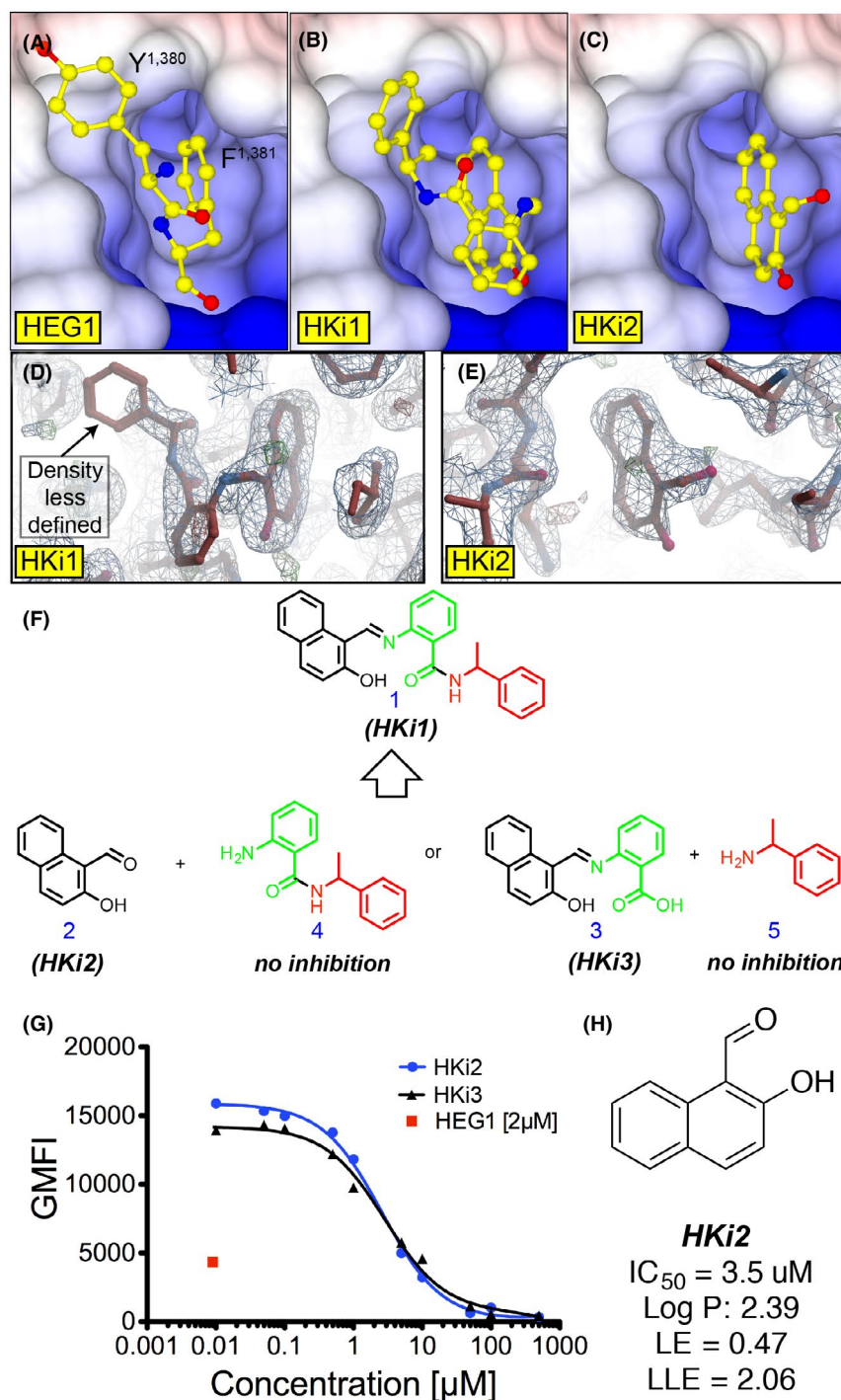


FIGURE 3 Structure guided HEG1–KRIT1 interaction inhibitors. (A–C) Surface charge representation of KRIT1 FERM domain crystal structures in complex with: (A) the HEG1 cytoplasmic tail highlighting the C-terminal Tyr-Phe sitting in the binding pocket (PDB ID: 3u7d); (B) HKi1; and (C) HKi2. Both small-molecule inhibitors HKi1 and HKi2 are sitting in the HEG1 binding pocket of KRIT1. (D–E) Electron density map of the KRIT1 FERM domain bound to: (D) HKi1; and (E) HKi2. Refined 2F0–FC map (blue) and F0–FC at 1 σ and 3 σ respectively (red and green). The small naphthalene of HKi1 and HKi2 show good electron density in the HEG1 binding pocket, whilst the electron density for the benzylamine moiety of HKi1 is less defined. (F) Chemical structure of HKi1 constituents. (G) Competition binding curve of 70 nM EGFP–KRIT1 FERM domain binding to 150 nM HEG1 on the beads with increasing amounts on HKi2 and HKi3. (H) Chemical structure of HKi2. LE and LLE are described in Figure 2A. The solubility of HKi2 in aqueous solution is largely improved.

3.4 | HKi2, an HKi1 fragment, blocks HEG1–KRIT1 protein–protein interaction

In addition to the relatively high lipophilicity and low aqueous solubility, HKi1 is also characterized by suboptimal values through efficiency metrics, such as the ligand efficiency (LE) and the lipophilic ligand efficiency (LLE)^{32,33} (Figure 2A). These characteristics suggest that this particular compound may be problematic as a starting point for hit-to-lead optimization studies. However, analysis of the complex structure (Figure 3B,D) suggested that while the naphthalene moiety of HKi1

may play an important role in determining the compound's binding and inhibitory activity, other fragments (e.g., the benzylamine) may not be as intimately involved in the binding to KRIT1. This observation led us to deconstruct HKi1 into its constituent fragments (Figure 3F) and investigate the ability of these fragments to inhibit the HEG1–KRIT1 in vitro. These studies confirmed that sub-structures containing the substituted naphthalene fragment, such as HKi2 and HKi3, produced inhibition of the HEG1–KRIT1 interaction, with IC_{50} values of 3.5 μM that are closely comparable to the IC_{50} value of the parent compound, HKi1 (Figure 3G). Interestingly, when we

TABLE 1 Data collection and refinement statistics for the KRIT1 FERM domain bound to Rap1 and small-molecule inhibitors: HKi1, HKi2, and HKi6.

	HKi1 (6OQ4)	HKi2 (6OQ3)	HKi6 (6UZK)
Data collection			
Space group	P2 ₁	P2 ₁	P2 ₁
Cell dimensions			
<i>a</i> , <i>b</i> , <i>c</i> (Å)	57.4, 77.4, 58.6	57.1, 76.8, 58.2	57.2, 77.1, 58.4
α , β , γ (°)	90.0, 91.6, 90.0	90.0, 92.3, 90.0	90.0, 91.6, 90.0
Resolution (Å)	58.6–1.75 (1.86–1.75) ^a	46.4–1.85 (1.96–1.85) ^a	50.0–1.92 (1.95–1.92) ^a
CC _{1/2}	99.9 (77.3) ^{a,b}	99.9 (78.0) ^{a,b}	99.1 (48.6) ^{a,b}
<i>R</i> _{meas}	0.042 (0.911) ^{a,b}	0.046 (1.406) ^{a,b}	0.113 (0.859) ^{a,b}
<i>I</i> / σ <i>I</i>	17.84 (1.71) ^{a,b}	16.49 (1.59) ^{a,b}	16.33 (1.00) ^{a,b}
Completeness (%)	99.5 (99.1) ^{a,b}	98.6 (98.0) ^{a,b}	94.0 (72.2) ^{a,b}
Redundancy	4.1 (4.0) ^{a,b}	3.78 (3.82) ^{a,b}	3.00 (1.9) ^{a,b}
Refinement			
Resolution (Å)	58.6–1.75	46.4–1.85	36.5–1.92
No. reflections	48536	40254	34351
<i>R</i> _{work} / <i>R</i> _{free}	22.6 / 26.4	24.4 / 29.2	22.0 / 28.6
No. atoms	4047	3936	3942
Protein	3844	3857	3819
Ligand/ion	63	46	48
Water	140	33	75
B-factors	38.4	52.2	48.1
Protein	41.7	52.6	48.3
Ligand/ion	52.8	50.2	50.0
Water	43.6	45.7	43.1
R.m.s deviations			
Bond lengths (Å)	0.002	0.003	0.002
Bond angles (°)	1.146	1.190	1.069
Ramachandran (%)			
Favored, allowed, outliers	98.1, 1.9, 0	97.4, 2.6, 0	97.0, 3.0, 0

^aHighest resolution shell is shown in parenthesis.

^bAs defined in XDS.

crystallized the KRIT1 FERM domain in complex with HKi2 (Figure 3C,E and Table 1), we observed that the naphthalene fragment retained the same binding mode within the HEG1 binding pocket on KRIT1 (Figure 3A) as noted in the HKi1 complex (Figure 3B). Given the relatively small size and reduced lipophilicity of HKi2 (Figure 3H), the LE, as well as the LLE, are considerably improved, suggesting that HKi2 could be considered as a promising starting point for further optimization.

3.5 | Evaluation of structure–activity relationship

To investigate the SAR of HKi2, a focused set of HKi2 analogues were either purchased or synthesized (Figure 4

and Supporting Information) and then tested in our in vitro flow cytometry binding assay. We found that compounds lacking the aldehyde moiety (compounds **9–15**) had no inhibitory activity detected by our screening assay (i.e., IC₅₀ of >500 μM), suggesting that the aldehyde plays a critical role. In addition, removal of the hydroxyl group (compound **7**) resulted in weak inhibition with an IC₅₀ of 75 μM, while no inhibition was observed for compound **8**, suggesting that the hydroxyl group at C2 is also preferred for inhibition activity. This observation is consistent with the presence of a hydrogen bond between the hydroxyl moiety of HKi2 and the side chain of Lys⁷²⁴ that was observed in the crystal structure (Figure 5A). Finally, opening of the fused bicyclic naphthalene ring of HKi2 to the corresponding non-fused phenylbenzene system (compound **6**) resulted in retention

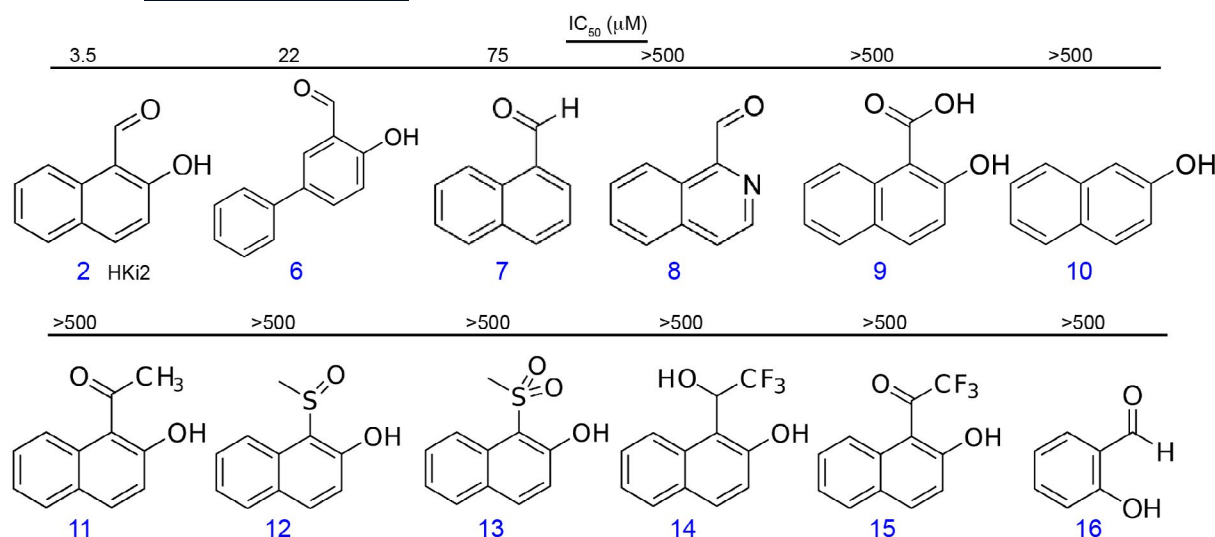


FIGURE 4 The aldehyde in position C1 and hydroxyl group in position C2 are important for HKi2 activity. The IC_{50} was measured using a flow cytometry-screening assay. >500 = no inhibition detected up to 500 μ M concentration thus $IC_{50} > 500$ μ M.

of moderate inhibition activity. However, with an IC_{50} of 22 μ M, salicylic aldehyde (compound **16**) did not exhibit detectable activity in the assay, suggesting that extended bicyclic aromatic systems may be ultimately preferred for inhibition of the HEG1–KRIT1 interaction. Thus, these results indicate that although the reactive carbonyl group in C1 is clearly required for inhibition of the HEG1–KRIT1 interaction, other features, such as the hydroxyl group in position C2 and a relatively extended aromatic system also play an important role.

3.6 | KRIT1 Lysine⁷²⁰ forms a covalent reversible bond (Schiff base) with the aldehyde of HKi2 for potent inhibition

The crystal structure shows that the HEG1-binding pocket of KRIT1 contains three lysines residues (Lys⁴⁷⁵, Lys⁷²⁴, and Lys⁷²⁰), which are located in the vicinity of the hydroxy-aldehyde of HKi2 when it is bound within the pocket (Figure 5A). Interestingly, mutation of any of the three KRIT1 lysines residues reduced the KRIT1 binding considerably to HEG1 in our assay (Figure 5B), suggesting that these residues are also important for the protein-protein interaction. Since HKi2 is equipped with a reactive carbonyl group, it is conceivable that this compound may inhibit the HEG1–KRIT1 interaction by engaging in covalent reversible binding (i.e., Schiff base formation) with one or more of these lysine residues. Interestingly, although the X-ray structure obtained for the KRIT1 FERM domain in complex with HKi2 (Figure 3C,E) did not reveal the presence of a covalent adduct, we have been able to obtain direct

evidence of Schiff base formation by trapping the adduct via sodium borohydride treatment (Figure 5C). Indeed, analysis of the samples via in-gel tryptic digestion followed by LC-MS/MS demonstrated that Lys⁷²⁰ is covalently modified by HKi2 (Figure 5D). This observation, combined with SAR results, strongly suggests that the inhibition produced by hydroxy naphthaldehyde compounds, such as HKi2, is in major part mediated by a covalent reversible binding of these compounds with the KRIT1 Lys⁷²⁰.

3.7 | HKi2 blocks the HEG1–KRIT1, but not the HEG1–PARD3 interaction

To further test the specificity of our compound to block the HEG1–KRIT1 interaction, but not other proteins, we looked at our previously published list of HEG1 interacting proteins²⁸ and found that partitioning defective 3 homolog (PARD3) was such an interactor. Indeed, using our HEG1 matrix, we were able to pull down at least three of the PARD3 isoforms from HUVEC lysates, confirming that PARD3 binds to the HEG1 cytoplasmic tail (Figure 5E). Importantly, PARD3 did not bind to the HEG1 Δ YF missing the last 2 C-terminal amino acids that are important for KRIT1 binding, suggesting that it binds to the same region of HEG1 as KRIT1. Finally, the addition of either HKi2 or 2-hydroxy-1-naphthoic acid (compound **9**) that does not block KRIT1 binding to HEG1 had no effects on PARD3 binding (Figure 5F and Figure S2). Thus, HKi2 appeared to be specific at blocking KRIT1 binding to HEG1 and did not affect PARD3 binding to the same region of the HEG1 tail.

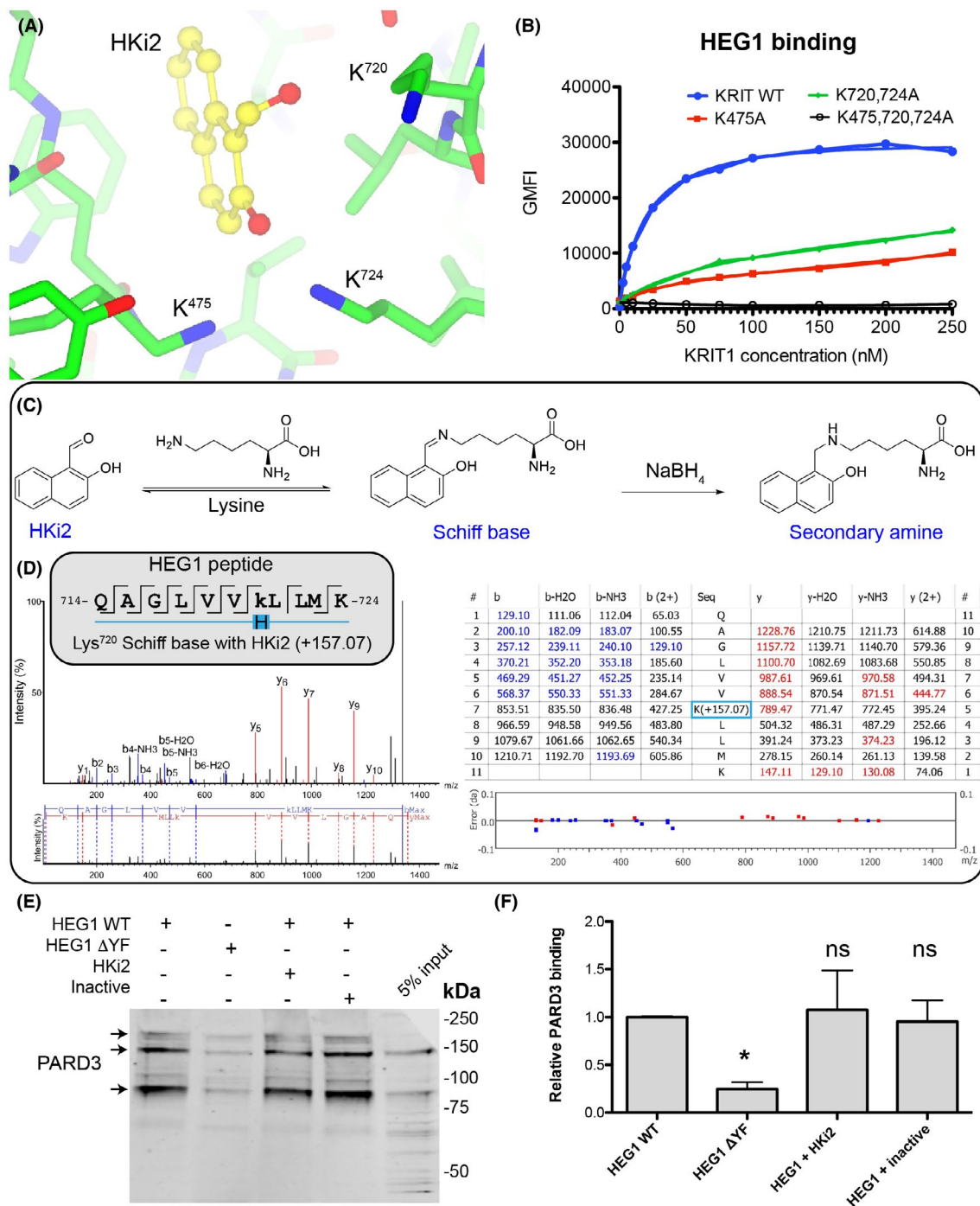


FIGURE 5 KRIT1 Lys⁷²⁰ forms a covalent reversible bond with the aldehyde of HKi2 and HKi2 does not block PARD3 binding to HEG1. (A) KRIT1 bound to HKi2 highlighting the position of three lysine residues near the HKi2 aldehyde. HKi2 is shown in yellow and KRIT1 residues in green. (B) All tested EGFP-KRIT1 FERM domain mutants tested had reduced HEG1 binding. (C) Expected lysine modification upon treatment with sodium borohydride to “trap” the Schiff base. (D) LC-MS/MS results. The searches in Peaks used a mass of 157.0653 (in monoisotopic mass) to lysine residues as variable modification. The tryptic peptide containing Lys⁷²⁰ showed such a mass for a lysine residue confirming that it forms a Schiff base with HKi2. (E) HUVEC lysates were incubated with either HEG1 WT or HEG1 ΔYF matrix and western blotted for PARD3. The mixture contained either DMSO, HKi2 or an inactive compound, 2-hydroxy-1-naphthoic acid (compound 9). The binding of PARD3 to HEG1 ΔYF is largely reduced in comparison to HEG1 WT, but neither HKi2 nor an inactive compound, 2-hydroxy-1-naphthoic acid, affected the binding. (F) Relative PARD3 binding from three independent experiments. Mean with SD are shown. ANOVA with a Tukey post hoc test: *, $p < 0.05$.

3.8 | HKi2 upregulates KLF4 and KLF2 levels in endothelial cells

To investigate the effects of acute inhibition of the endothelial HEG1–KRIT1 interaction, we used the human cerebral microvascular endothelial cell-line, hCMEC/D3.³⁴ Our group and others have shown that genetic inactivation or

knockdown of endothelial HEG1 or KRIT1 leads to the up-regulation of endothelial KLF4 and KLF2 expression.^{12–16} However, it is unknown whether disruption of the HEG1–KRIT1 interaction is sufficient to regulate expression of endothelial KLF genes. Our results showed that *KLF4* and *KLF2* mRNA levels were indeed upregulated following the addition of 25 μ M HKi2 for 12 h of treatment (Figure

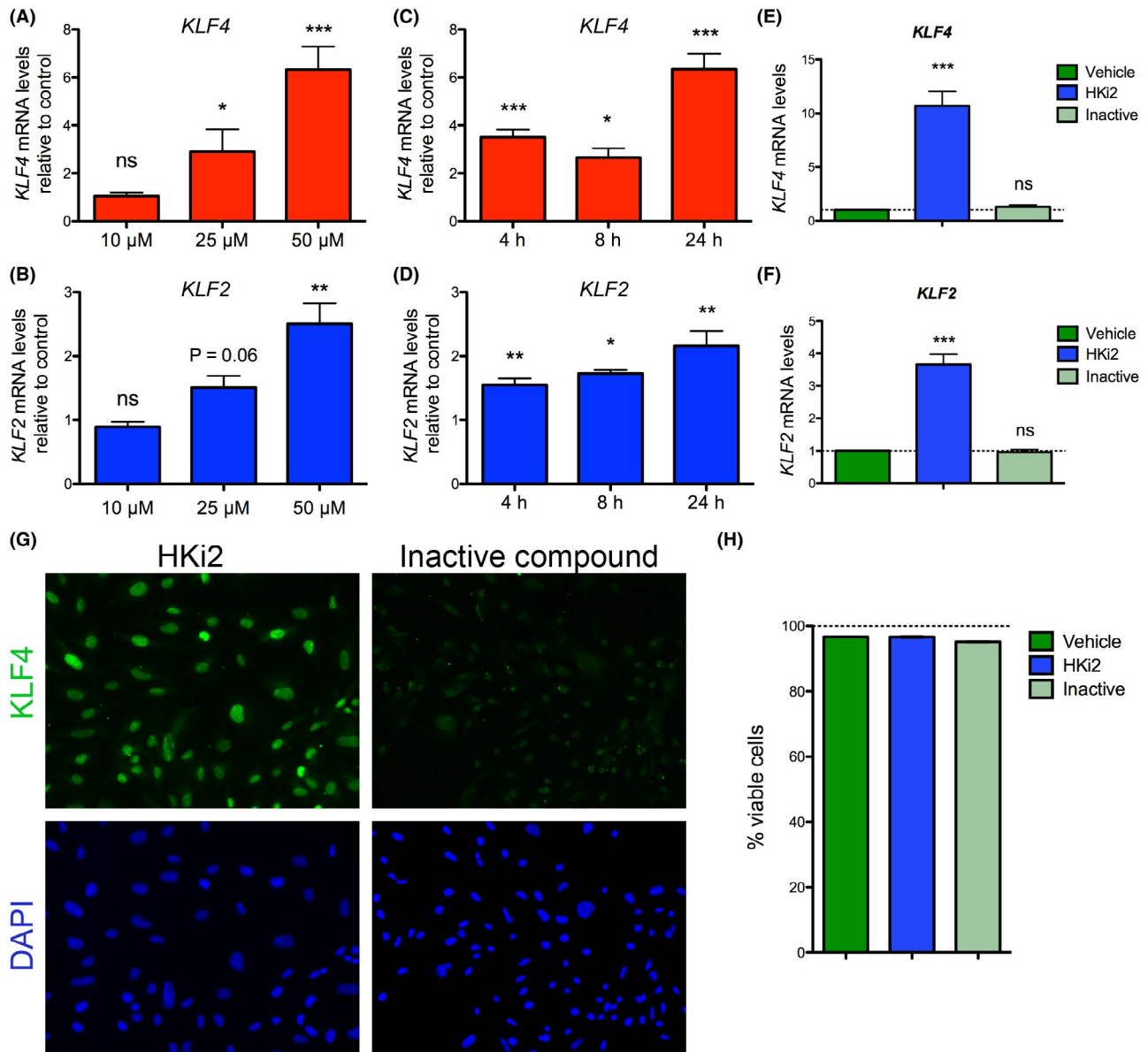


FIGURE 6 HKi2 treatment leads to KLF2 and KLF4 upregulation in endothelial cells. (A–F) hCMEC/D3 cells treated with HKi2 (50 μ M) or vehicle control and analyzed by qPCR for mRNA level. (A, B) Dose response of KLF4 and KLF2 mRNA expression at indicated doses for 12 h. HKi2 induces KLF4 and KLF2 mRNA expression at indicated concentrations. (C, D) Timecourse, HKi2 induces a rapid and sustained upregulation of KLF4 and KLF2 mRNA expression. (E, F) HKi2 treatment for 4 h upregulated (E) KLF4, and (F) KLF2, and an inactive compound, 2-hydroxy-1-naphthoic acid (50 μ M) (compound 9), did not. (A–F) Bar graphs represent mRNA levels relative to vehicle control \pm SEM with: (A–D) $n = 3$, t test and (E, F) $n = 4$, one-way ANOVA. *, $p < 0.05$; **, $p < 0.01$; ***, $p < 0.001$. (G) Representative images of hCMEC/D3 cells treated for 12 h with HKi2 (50 μ M) or inactive compound (50 μ M), 2-hydroxy-1-naphthoic acid, and analyzed by Immunofluorescence for KLF4 protein levels. KLF4 expression is increased after treatment with HKi2. (H) Cell viability as assessed by flow cytometry using Propidium Iodide staining, no significant difference between vehicle, HKi2 and inactive compound, 2-hydroxy-1-naphthoic acid. Percentage of viable cells \pm SEM. $n = 3$, one-way ANOVA.

TABLE 2 RNA-seq analysis of HUVEC transcriptome after treatment with HKi2. List of the top 50 up- or down-regulated genes in HUVEC from treatment with HKi2 (75 μ M) for 24 h compared with vehicle treatment (DMSO).

Upregulated				Downregulated			
#	Symbol	Log2(HKi3-CTRL)	p	#	Symbol	Log2(HKi3-CTRL)	p
1	ATP6V0D2	5.477856011	3.80E-09	1	DEPP1	-6.235526118	6.63E-42
2	IL13RA2	5.280396025	1.44E-11	2	FAM111B	-4.708958211	5.78E-11
3	BEX2	5.262346672	3.52E-11	3	ADGRF5	-4.299774707	5.48E-08
4	ADM2	4.999541481	2.95E-13	4	RRM2	-4.290514953	5.19E-31
5	ERFE	4.670090763	1.75E-07	5	PPP1R16B	-4.242177919	8.19E-16
6	ATF3	4.47211673	7.62E-27	6	LRRC17	-4.073077627	2.68E-05
7	CYP1B1	4.208970731	6.65E-05	7	GIMAP8	-4.048995565	5.44E-19
8	ZNF365	4.146090877	1.29E-05	8	LYVE1	-3.891285503	2.82E-44
9	SPX	4.124571508	3.66E-05	9	MCM10	-3.784113085	6.89E-08
10	TSLP	3.821600944	0.000453641	10	CD34	-3.763788118	0.000341658
11	FAM129A	3.812798736	1.40E-23	11	DIPK2B	-3.729793318	3.60E-29
12	DDIT3	3.687856752	1.07E-100	12	ZNF367	-3.523248117	2.55E-06
13	TMIE	3.588942589	0.00240504	13	E2F1	-3.481468554	2.98E-20
14	LURAPIL	3.554858667	6.02E-18	14	PALD1	-3.477140385	0.001575678
15	PTGS2	3.554108003	5.38E-57	15	MCM4	-3.445247916	1.90E-26
16	TRIB3	3.552042645	9.61E-244	16	GIMAP4	-3.430855989	9.00E-80
17	HSPA6	3.51809314	0.004320318	17	ORC1	-3.425105138	1.41E-07
18	ULBP1	3.506015509	0.00012681	18	EMCN	-3.401070791	1.12E-24
19	NGFR	3.411996292	0.006714317	19	ANGPT2	-3.379871248	6.29E-14
20	RAB39B	3.308505038	0.009607606	20	SOX18	-3.342147498	1.30E-47
21	HIST2H2BE	3.267927681	2.18E-05	21	TNFSF15	-3.330365738	2.38E-12
22	CHAC1	3.249494666	8.71E-22	22	PDGFB	-3.322631501	2.91E-08
23	CLDN1	3.247740584	0.004494556	23	TM4SF18	-3.304488314	1.40E-11
24	ARRDC4	3.232886935	0.00459744	24	EXO1	-3.29610072	4.85E-06
25	DDIT4	3.209247671	6.72E-30	25	TFPI2	-3.235631694	5.46E-75
26	PTPRH	3.204827931	0.000250073	26	CSGALNACT1	-3.198493959	2.11E-05
27	SLC6A9	3.150494146	0.000731629	27	GBP4	-3.162775585	0.000328915
28	STC1	3.115477634	7.96E-123	28	FABP4	-3.14649607	0.000575794
29	THBD	3.058867474	7.06E-69	29	POLE2	-3.139091857	1.60E-05
30	BMP2	3.047956517	1.16E-125	30	DHFR	-3.103398997	5.20E-12
31	RND3	3.03479447	2.36E-143	31	CCNE2	-3.100192827	0.000441624
32	DUSP8	3.019900682	0.000873573	32	GIMAP7	-3.083914904	1.16E-16
33	HMOX1	2.985725279	0	33	DHCR24	-3.055244718	5.54E-45
34	NKAPL	2.843490463	0.001444862	34	NES	-3.033921643	1.70E-25
35	SESN2	2.813008185	5.04E-35	35	FADS2	-3.025390376	1.70E-11
36	HOXB9	2.78609355	0.023176326	36	CCL2	-2.993115714	0.000558785
37	CEBPB	2.770664242	2.11E-27	37	MCM6	-2.991955103	3.24E-23
38	VIP	2.766834534	0.000423314	38	CASP12	-2.956866649	0.011749482
39	HGFAC	2.703575854	0.015631435	39	MYBL2	-2.935738455	2.81E-30
40	HIST1H2AC	2.701498983	1.63E-07	40	RARB	-2.934472013	3.92E-23
41	TMEM45B	2.668658073	0.00125267	41	CAV1	-2.932329697	4.04E-302

(Continues)

TABLE 2 (Continued)

Upregulated				Downregulated			
#	Symbol	Log2(HKi3-CTRL)	p	#	Symbol	Log2(HKi3-CTRL)	p
42	AOC2	2.628442433	0.009785157	42	TYMS	-2.92440964	3.85E-13
43	SAT1	2.595140535	5.52E-152	43	GDF3	-2.917710233	0.007674853
44	PAPPA2	2.592159089	0.001619709	44	E2F2	-2.915902665	0.013157616
45	CXCL2	2.53521089	3.26E-05	45	CDCA7	-2.909478486	6.12E-07
46	RASGRF2	2.521366756	6.52E-05	46	LXN	-2.894687047	9.20E-64
47	C9orf64	2.500174013	0.000798624	47	TCF19	-2.894445982	7.64E-16
48	BEX1	2.489060141	0.043114966	48	CYP26B1	-2.880574011	0.002816822
49	PPP1R15A	2.467383493	8.78E-174	49	MCM2	-2.832945637	1.12E-11
50	GEM	2.452829088	4.26E-13	50	APLN	-2.822754099	2.44E-169

6A,B). Increasing the concentration of HKi2 led to further upregulation of *KLF4* and *KLF2* mRNA levels. While the upregulation of *KLF4* mRNA levels (~6.5-fold increase at 50 μ M) was profound, when compared with controls (Figure 6A), the changes in *KLF2* mRNA levels (~2.3-fold increase at 50 μ M) were less dramatic, but still significant (Figure 6B). We also noted that incubation of hCMEC/D3 cells with 50 μ M HKi2 induced a rapid upregulation of *KLF4* (~3.5-fold increase, Figure 6C) and *KLF2* (~1.5-fold increase, Figure 6D) as early as 4 h, which continued to increase over the treatment course ending at 24 h. An even greater increase in *KLF4* levels (~6-fold increase) were detected following treatment with HKi2 for 24 h (Figure 6C). Cells in culture require serum, which contains scavengers such

as albumin and other proteins that can reduce the activity of small molecules such as HKi2. Thus, this could explain why we needed higher concentrations in cell culture experiments than in biochemical or zebrafish studies. Importantly, hCMEC/D3 cells treated for 4 h with 50 μ M of a structurally similar analog of HKi2 (compound 9) that failed to block the HEG1–KRIT1 interaction, did not elevate *KLF4* or *KLF2* (Figure 6E,F respectively). This result is a biological read-out indicating that HKi2 is specific in its blockade of the HEG1–KRIT1 interaction since a similar, but inactive derivative of the compound had no biological effect. We next assessed whether an increase in *KLF4* mRNA levels correlates with an increase in *KLF4* protein expression in hCMEC/D3 treated with HKi2 (50 μ M). Importantly, knowing that

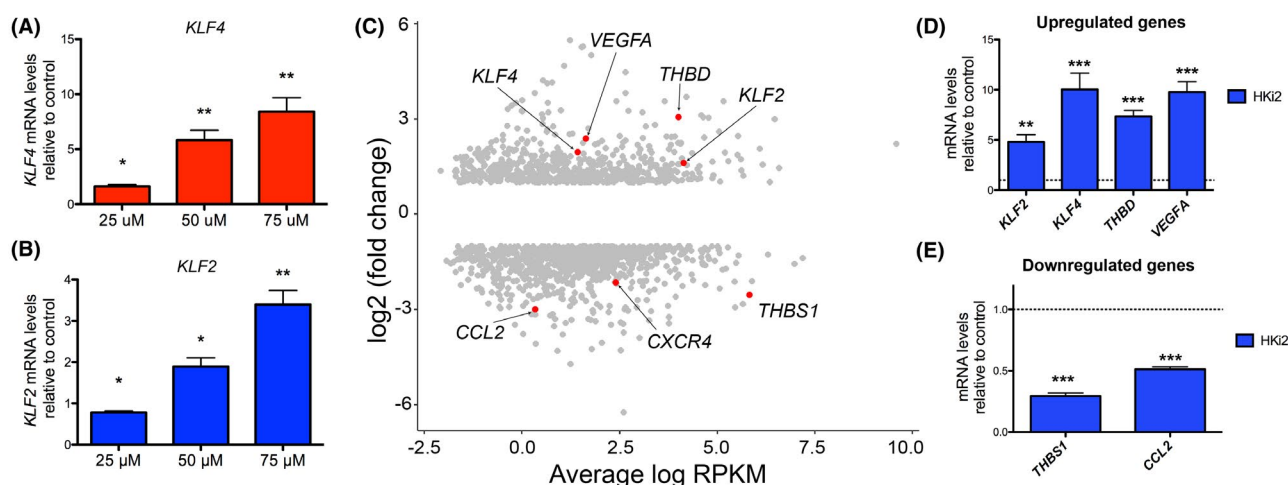


FIGURE 7 HKi2 treatment leads to *KLF4* and *KLF2* upregulation, and their important transcriptional targets. (A–E) HUVEC treated with HKi2 (75 μ M) or vehicle control for 24 h. (A,B) Dose response of *KLF4* and *KLF2* mRNA expression as determined by qPCR at indicated doses. HKi2 induces *KLF4* and *KLF2* mRNA expression at indicated concentrations. Bar graphs represent mRNA levels relative to vehicle control \pm SEM ($n = 3$, t test). *, $p < 0.05$; **, $p < 0.01$; ***, $p < 0.001$. (C–E) Expression levels of differentially expressed genes upon HKi2 treatment. (C) Scatter plot of RNA-Seq data; reads per kilobase of transcript per million mapped reads (RPKM) of individual transcripts are represented on a log2 scale. A few of the most highly suppressed and up-regulated genes are labeled. (D,E) qPCR of representative: (D) upregulated; and (E) downregulated genes ($n = 4$, one-way ANOVA). ***, $p < 0.001$.

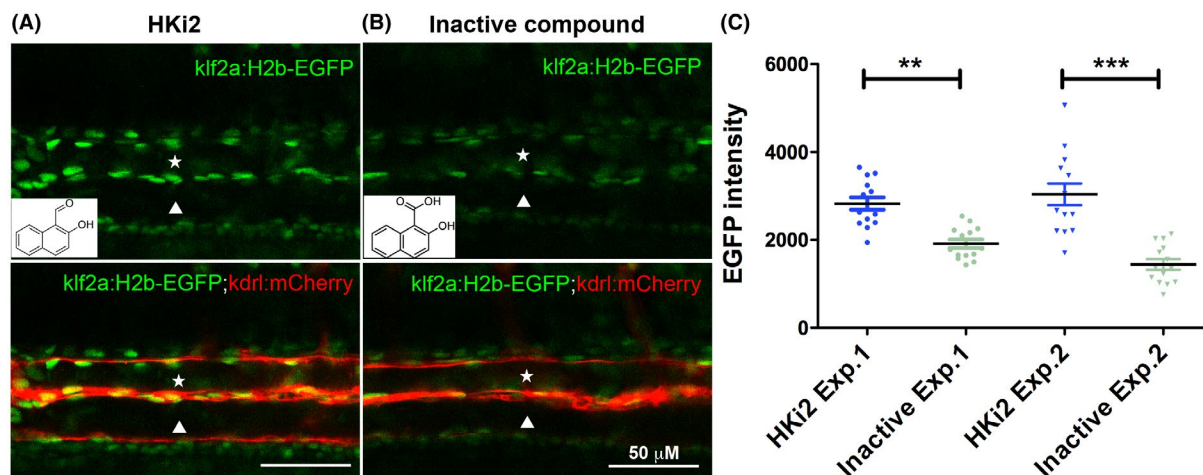


FIGURE 8 HKi2 induces expression of *klf2a* in arterial and venous endothelium in zebrafish. (A,B) Tg(*klf2a*:H2b-EGFP;*kdrl*:mCherry) zebrafish embryos *klf2a* expression reporter (EGFP) and endothelial cells labeling (mCherry) after treatment with: (A) 4 μ M HKi2; or (B) 4 μ M inactive compound, 2-hydroxy-1-naphthoic acid (compound 9). The compounds were added at 26 hpf, and images were taken at 30 hpf. The trunk vessels were scanned using Airyscan. Star and square indicate dorsal aorta and posterior cardinal vein, respectively. Lateral view with anterior to the bottom and dorsal to the top. (C) Quantification of the EGFP fluorescence intensity using imageJ. A total of seven nuclei were analyzed per embryo, two HKi2 treated and two inactive compound embryos per experiment, and results from two independent experiments were analyzed. (n = 2, one-way ANOVA). **, $p < 0.01$; ***, $p < 0.001$.

the KLF4 mRNA is upregulated after 4 h of treatment with HKi2, we looked at endothelial KLF4 protein expression by immunofluorescence after 12 h treatment to allow sufficient time for protein production. We found that HKi2 induced an upregulation of KLF4 protein, as assessed by immunofluorescence staining (Figure 6G). Finally, we looked at cell viability using propidium iodide staining after 24 h of HKi2 treatment and found no statistical difference between the cells treated with: HKi2; an inactive compound (compound 9); or vehicle alone (Figure 6H). Therefore, the KLF4 and KLF2 upregulation does not appear to be due to potential toxicity of HKi2 on the cells, and acute inhibition of the endothelial HEG1–KRIT1 interaction with HKi2 is sufficient to elevate endothelial KLF4 and KLF2 expression at the mRNA and protein levels under static conditions, while a structurally similar inactive analog of HKi2 has no effect.

3.9 | HKi2 upregulates KLF4 and KLF2 target genes in endothelial cells

Next, we used primary human umbilical vein endothelial cells (HUVEC) to study the effect of HKi2 on endothelial gene expression in a second source of endothelial cells to confirm our previous results. We observed that similar to hCMEC/D3 cells, HUVEC-treated with HKi2 upregulated both *KLF4* and *KLF2* mRNA levels in a dose-dependent manner (Figure 7A,B). Importantly, HKi2 treatment did not affect KRIT1 or HEG1 mRNA levels (Figure S3). We next used genome-wide RNA sequencing (RNA-seq) to

further characterize the effects of inhibiting the HEG1–KRIT1 interaction at the transcriptional level. Deep sequencing of cDNA from HUVEC after 24 h treatment with HKi2 (75 μ M), which showed maximal effect on *KLF4* and *KLF2* expression (Figure 7A,B), revealed that disruption of the HEG1–KRIT1 protein interaction caused a dramatic change in the overall gene expression profile in endothelial cells (Figure 7C and Table 2). We identified 457 genes differentially expressed between HKi2 treatment and vehicle control (corrected $P < 0.05$, ≥ 2.5 -fold change). The most notable changes included *KLF4* and *KLF2* target genes, with upregulation of *VEGFA* (encoding vascular endothelial growth factor A, VEGF-A), and *THBD* (encoding thrombomodulin, TM) (Figure 7C,D). Among the most notably downregulated were genes encoding receptors that regulate angiogenesis or secreted proteins, including *THBS1* (encoding thrombospondin1, TSP1), *CXCR4* (encoding C-X-C chemokine receptor type 4, CXCR-4), and *CCL2* (encoding monocyte chemoattractant protein, MCP1) (Figure 7C,E). Importantly, using the same conditions, we tested two structurally similar compounds that were shown to be inactive in blocking the HEG1–KRIT1 interaction in vitro (compounds 9 and 10), and found no significant effects on HUVECs gene expression by RNA-Seq (Data not shown) compared to vehicle control samples. These results further confirm that the effects of HKi2 are ascribable to the blockade of the endothelial HEG1–KRIT1 interaction, with the resulting gene expression changes revealing a similar profile to cells deficient for KRIT1.

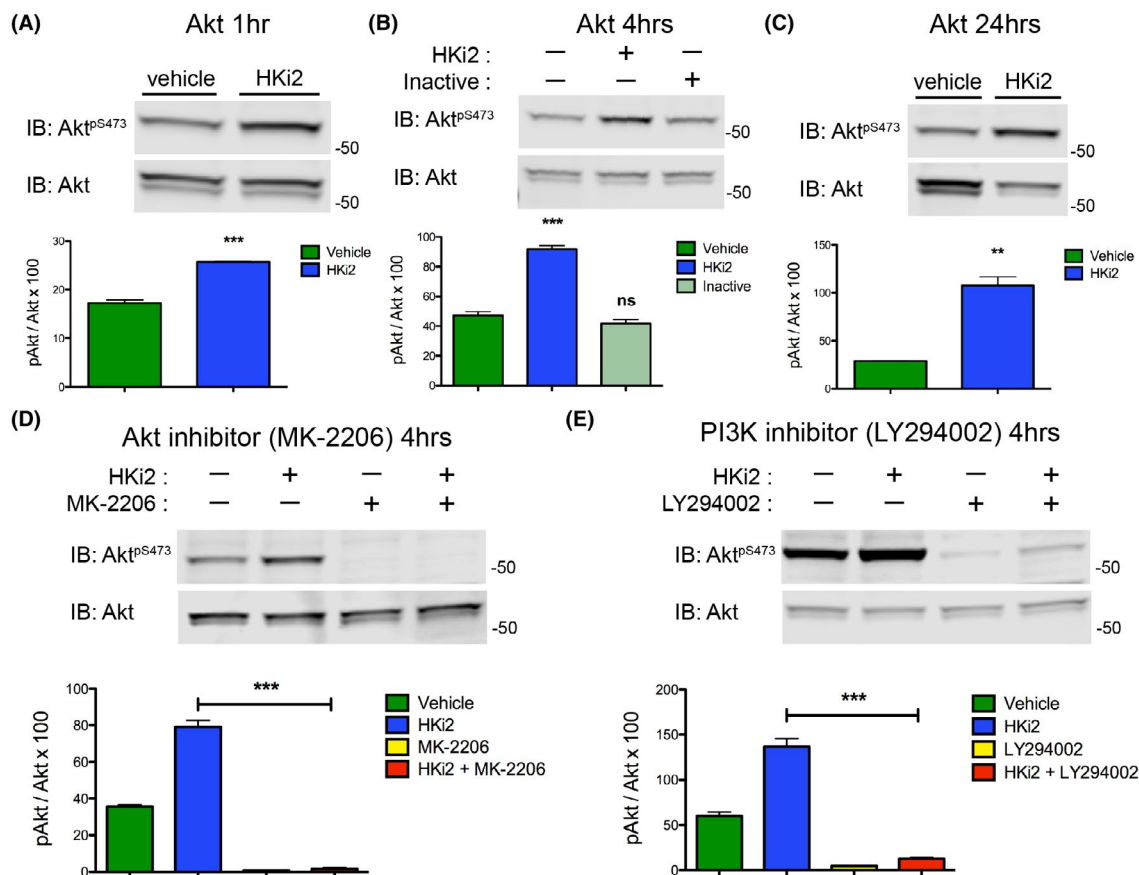


FIGURE 9 HKi2 treatment increases Akt phosphorylation at S⁴⁷³ that is dependent on PI3K activity. (A-E) hCMEC/D3 cells treated with HKi2 (50 μ M) or vehicle control. Cells lysates were analyzed by western blot for Akt and p-Akt S⁴⁷³ protein levels. (A) HKi2 treatment for 1 h activated Akt signaling. (B) HKi2 treatment for 4 h activated Akt signaling and an inactive compound (50 μ M), 2-hydroxy-1-naphthoic acid, did not (compound 9). (C) HKi2 treatment for 24 h activated Akt signaling, but the total levels of total Akt were going down. (D,E) Blocking the kinase activity of (E) Akt with MK-2206 (20 μ M) and (F) PI3K with LY294002 (10 μ M) blunted the activation of Akt by HKi2. (A-H) Bar graphs represent average \pm SEM (n = 4), with (A,C) *t* test, and (B,D,E) one-way ANOVA. *, *p* < 0.05; **, *p* < 0.01; ***, *p* < 0.001.

3.10 | HKi2 induces expression of *klf2a* in arterial and venous endothelium in zebrafish

We next addressed the effect of acute inhibition of the HEG1–KRIT1 protein complex in vivo. For this, we used zebrafish embryos in which the KRIT1–HEG1 interaction is conserved,^{2,7,13} and we could utilize the unique advantages of optical transparency that allow visualization for individual genes using non-invasive imaging.³⁵ Here we also took advantage of a transgenic *klf2a* reporter line, *Tg(klf2a:H2B-EGFP)*, which consists of a 6-kb fragment of the *klf2a* zebrafish promoter driving the expression of the nuclear-localized histone-EGFP fusion protein.^{30,31} This line was combined with the *Tg(kdrl:mCherry)* to label the endothelium with red fluorescence - *Tg(klf2a:H2B-EGFP;kdrl:mCherry)*. Our results showed that zebrafish embryos treated with 4 μ M HKi2 for 4 h at 26 h post-fertilization (hpf), displayed an increase of EGFP in the arterial and venous endothelium (labeled with mCherry) (Figure 8A). Importantly, no effects on nuclear EGFP were observed in embryos treated

with an inactive compound (Figure 8B) or control vehicle DMSO (data not shown). We quantified the nuclear EGFP intensity and found a significant difference in comparison with the inactive compound from two independent experiments (Figure 8C). These data show that blocking the HEG1–KRIT1 protein complex triggers an elevation of KLF2 expression in vivo in the presence blood flow.

3.11 | HKi2 increases Akt activity in endothelial cells in a PI3K-dependent manner

To further investigate the effects of acute inhibition of the endothelial HEG1–KRIT1 interaction by HKi2, we looked at Akt activation state, which has been implicated in the regulation of endothelial KLF expression.^{20,36,37} hCMEC/D3 cells treated with the small-molecule HKi2 (50 μ M) for 1 h significantly induced a 1.5-fold increase in Akt activation, as assessed by western blot analysis of pAkt-S⁴⁷³

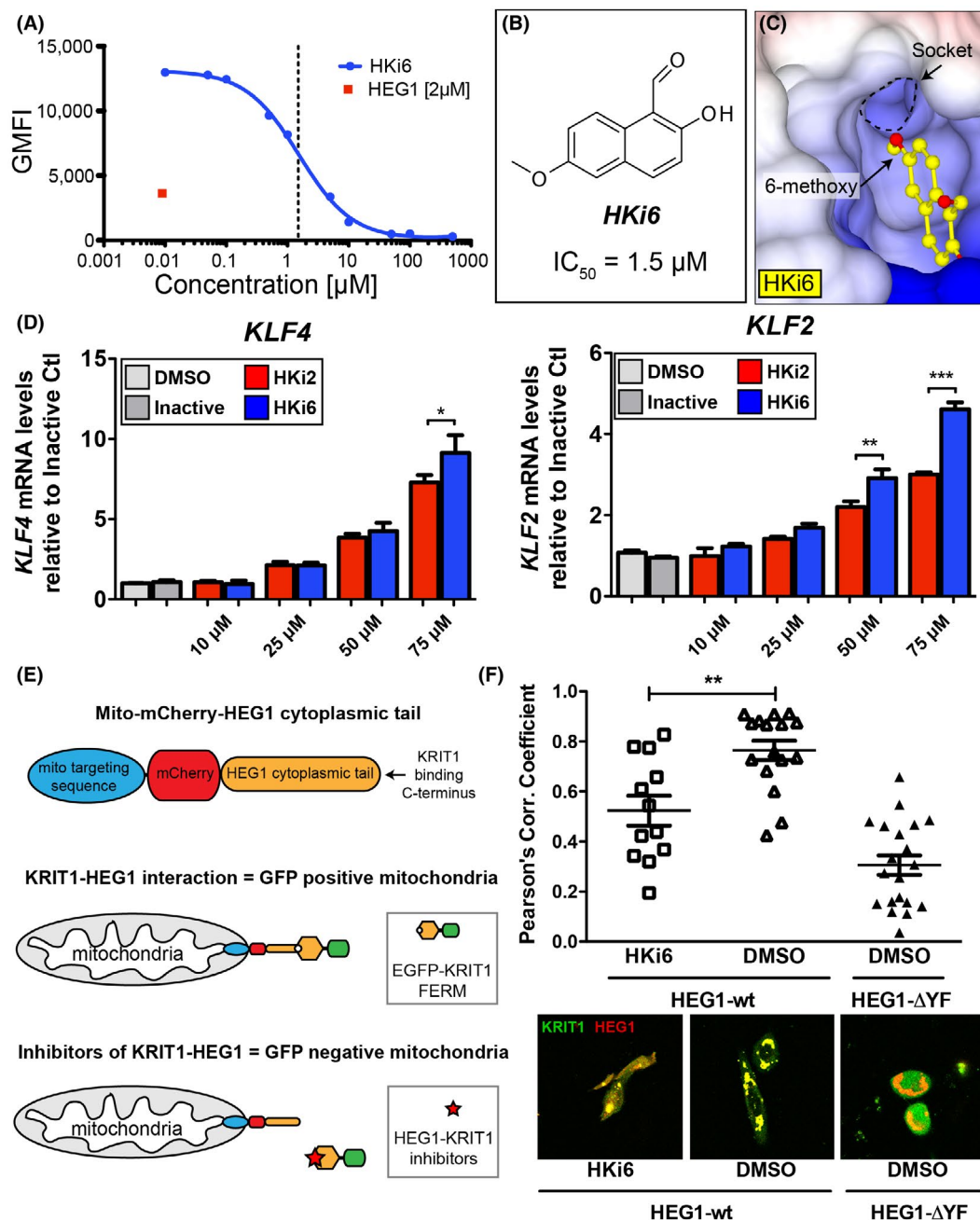


FIGURE 10 The HEG1-KRIT1 interaction can be disrupted in cells by a small-molecule inhibitor HKi6. (A) Competition binding curve of 70 nM EGFP-KRIT1 FERM domain binding to 150 nM HEG1 on the beads with increasing amounts on HKi6. (B) Chemical structure of HKi6. (C) Surface charge representation of KRIT1 FERM domain crystal structures in complex with HKi6 sitting in the HEG1 binding pocket of KRIT1 (PDB ID: 6uzk). (D) Dose response of KLF4 and KLF2 mRNA expression at indicated doses for 4 h. HKi6 has increased potency in upregulating KLF4 and KLF2 mRNA expression in HUVECs, compared to the same dose of HKi2. Inactive compound was at (75 μM) treatment. Bar graphs represent average \pm SEM ($n = 4$), one-way ANOVA. *, $p < 0.05$; **, $p < 0.01$; ***, $p < 0.001$. (E) Schematic representation of a novel assay to assess the HEG1-KRIT1 interaction in living cells. Mito-mCherry-HEG1 is targeted to mitochondria and the recruitment of EGFP-KRIT1 FERM domain to HEG1 can be measured by colocalization. (F) Small-molecule inhibitor HKi6 prevents the interaction of KRIT1 with HEG1 in living cells. EGFP-KRIT1 is colocalized with mCherry-HEG1 wild-type at the mitochondria, but not with the HEG1- ΔYF missing the last 2 C-terminal amino acids that are important for KRIT1 binding (negative control). Bar graphs represent the Pearson colocalization coefficient relative to DMSO vehicle control. Average \pm SEM (one-way ANOVA). **, $p < 0.01$.

(Figure 9A). Since the KLF4 and KLF2 mRNA expression is upregulated after 4 h treatment, we looked at Akt phosphorylation at 4 h and found a 2-fold increase (Figure

9B). Importantly, a structurally similar analog of HKi2, the 2-hydroxy-1-naphthoic acid (compound 9) that failed to block HEG1-KRIT1 interaction, did not elevate Akt activity.

We also looked after 24 h treatment and found a 3.7-fold increase, however we observed a significant downregulation of the total Akt levels (Figure 9C). We judged that the 4 h was the best timepoint for following studies of the Akt activity after treatment with HKi2. We next tested an Akt inhibitor, MK-2206, and found that this compound can indeed prevent the increase in Akt phosphorylation due to HKi2 treatment (Figure 9D). Since Akt needs PI3K activity to be activated, we next tested a PI3K inhibitor, LY294002, which also prevented an increase in Akt signaling following acute inhibition of endothelial HEG1–KRIT1 protein interaction by HKi2 (Figure 9E).³⁸ Thus, acute inhibition of the endothelial HEG1–KRIT1 interaction with HKi2 increases Akt activity, and can be reversed by blocking either AKT or PI3K activity.

3.12 | Small-molecule inhibitor HKi6 has increased potency and can disrupt the HEG1–KRIT1 interaction in cells

Evaluation of the X-ray structures of HKi1 and HKi2 bound to KRIT1 (Figure 3B,C) indicated that further growth originating at position 6 of the naphthalene ring could be exploited to increase complementarity. Evaluation in the biochemical assay identified the 6-methoxy derivative (HKi6) with an improved IC₅₀ of 1.5 μ M in comparison with HKi2 (Figure 10A,B). Importantly, the crystal structure of the KRIT1 FERM domain bound to HKi6 (Figure 10C) confirmed that the methoxy group in position 6 is projecting towards an adjacent socket that was originally identified in the HKi2-bound structure. Furthermore, the crystal structure data reveal that the pendant methoxy group establishes an H-bond with the backbone of Gln⁴⁷³. As shown in Figure 10D, HKi6 also appears to have increased potency in upregulating the *KLF2* and *KLF4* gene expression in HUVECs, compared with the same dose of HKi2.

We have previously used a mitochondrial (mito) targeting sequence fused to a fluorescent protein, mCherry, and the HEG1 cytoplasmic domain (mito-mCherry-HEG1) to re-localize Rasip1 to mitochondria.²⁸ This experimental setup allowed us to detect the HEG1–Rasip1 interaction in cells and establish that the HEG1 tail can control the localization of Rasip1. We used a similar strategy here to ask whether KRIT1 and HEG1 indeed interact in living cells, and whether that interaction can be disrupted by our HKi compounds. We co-transfected CHO cells with mito-mCherry-HEG1 cytoplasmic tail and EGFP–KRIT1 FERM domain (Figure 10E). Importantly, targeting of mito-mCherry-HEG1 to mitochondria successfully recruited EGFP–KRIT1 FERM domain, as shown by the high colocalization coefficient measured, demonstrating for the first time that HEG1 can specify the localization of KRIT1 in cells (Figure 10F). Additionally, mito-mCherry-HEG1– Δ YF, which cannot bind KRIT1, did not show colocalization with EGFP–KRIT1 at the mitochondria, indicating a lack of binding, as

expected. Importantly, 75 μ M HKi6 significantly reduced the localization of EGFP–KRIT1 to wild-type HEG1 tail at the mitochondria, indicating that HKi6 disrupts the HEG1–KRIT1 interaction in living cells. This new derivative, HKi6, with 3-fold higher affinity for KRIT1, is evidence that these HKi small molecules can be further modified and honed to produce stronger and more specific effects on the KRIT1–HEG1 complex with the goal of elucidating the key signaling pathways regulated by this interaction.

4 | DISCUSSION

HEG1 cytoplasmic tail binds directly to the KRIT1 FERM domain through discrete and unique interactions⁵ and the loss of endothelial HEG1 or KRIT1 increases *KLF4* and *KLF2* gene expression.^{7,12–16} However, the biological effect of inhibiting endothelial HEG1–KRIT1 interaction remains incompletely understood due to the lack of tools to block their interaction while keeping their own integrity. In this study, we evaluated the pharmacological inhibition of the endothelial HEG1–KRIT1 interaction as a new tool to identify downstream signaling pathways of the acute HEG1–KRIT1 protein complex disruption. We developed a reliable and quantitative assay to study the HEG1–KRIT1 protein interaction by flow cytometry. High throughput screening, followed by SAR of the most promising hits led to the identification of a series of fragment-like hydroxy naphthaldehyde HEG1–KRIT1 inhibitors. X-ray co-crystal structure studies of KRIT1 FERM domain in complex with HKi1, HKi2, and HKi6 demonstrate that the naphthalene fragment retained the same binding mode within the HEG1 binding pocket on KRIT1. Recent studies found that fragments of ligands that fully overlap with the strongest hot spot generally retain their position and binding mode when the rest of the molecule is removed.³⁹ The low μ M IC₅₀ values of these smaller fragments, especially HKi2, appears to be considerably more potent (i.e., approximately ~100 to 1000 times) than those typically observed for low MW fragments that can establish only a few non-covalent interactions with the target protein. This observation suggests that the relatively reactive carbonyl moiety of HKi2 may undergo covalent reversible binding, (i.e., formation of a Schiff base), with the KRIT1 FERM domain, as previously observed for peptidyl aldehydes inhibitors of Src homology 2 (SH2) domains.⁴⁰ Among the 20 proteinic amino acids, the side chains of lysine and arginine are capable of forming covalent reversible interactions with aldehydes (typically in the form of an imine or enamine adduct). Indeed, the crystal structure showed that the HEG1 binding pocket of KRIT1 contains three lysines residues positioned to engage the aldehyde of HKi2 in covalent reversible binding. Although the electron density for these lysines side-chains could not show definitively

which of the three was engaging the aldehyde, sodium borohydride-mediated trapping of the imine adduct followed by in-gel tryptic digest and LC-MS/MS ultimately identified Lys⁷²⁰ as the residue involved in the Schiff base formation with HKi2. Moreover, SAR studies confirmed that the reactive carbonyl group of HKi2 is required for inhibition of the HEG1–KRIT1 interaction. Equally important, comparison of HKi2 with closely related but inactive congeners, such as 2-hydroxy-1-naphthoic acid (compound **9**), suggests that HKi2 exhibits specificity in blocking the HEG1–KRIT1 interaction in both cultured cells, as well as zebrafish studies. Thus, taken together, these results strongly suggest that HKi2 is a bona fide fragment-like inhibitor of the HEG1–KRIT1 interaction that can be used in future studies to elucidate the signaling events regulated by this protein complex.

The binding of KRIT1 FERM domain to the most C-terminal region in HEG1 mediates KRIT1 localization and function in EC. Here we show for the first time in a living cell/organism that targeting mito-mCherry-HEG1 to mitochondria localized exogenous EGFP-KRIT1 FERM domain to these organelles in cells. Mapping studies identified the most C-terminal portion of HEG1(1380–1381) cytoplasmic tail as the critical region for KRIT1 binding. Deletion of this site, (HEG1 Δ YF), abrogated the capacity of HEG1 to bind KRIT1 and to recruit it to mito-mCherry-HEG1. Our experiments performed using this assay show that the HEG1–KRIT1 interaction can indeed be blocked in living cells with HKi6, the newest of our inhibiting compounds with increased affinity for KRIT1. HKi6 has improved IC₅₀ value compared to the original compound in our assay and also has increased potency in upregulating the KLF2 and KLF4 genes expression in HUVECs, compared with the same dose of HKi2. Thus, in a novel colocalization assay in vitro, we show physical evidence that the HEG1–KRIT1 complex can be disrupted in cells by our small-molecule inhibitors.

Next, we hypothesized that pharmacological inhibition of the HEG1–KRIT1 protein interaction could be used to study acute signaling events regulated by this protein complex. It is well documented that genetic inactivation or knockdown of endothelial HEG1 or KRIT1 under static conditions results in upregulation of *KLF4* and *KLF2*, which are genes normally induced by laminar blood flow.^{12–16,18,19} Indeed, acute inhibition of the endothelial HEG1–KRIT1 interaction with HKi2 under static conditions was also sufficient to rapidly upregulate in a time- and dose-dependent manner *KLF4* and *KLF2* mRNA expression, as well as their direct target genes. Furthermore, zebrafish treated with HKi2 showed increased *klf2a* expression within the vascular endothelium in the presence of flowing blood. These data establish that inhibiting endothelial HEG1–KRIT1 interaction leads in part to similar outcomes as loss of HEG1 or KRIT1, and mimics many of the transcriptional effects of laminar blood flow. Importantly, the gain of endothelial MEKK3 activity has been associated with the upregulation

of KLF4 and KLF2 in the cerebral cavernous malformation (CCM) disease.^{12–14} MEKK3 interacts with the CCM protein complex (composed of HEG1–KRIT1–CCM2–PDCD10) by binding directly to CCM2,^{17,41} and loss of CCM proteins results in an increase in MEK5–ERK5–MEF2 mechanotransduction pathway.^{12–14,18,19,41} Furthermore, in zebrafish, both *heg1* and *krit1* play crucial roles in controlling the sensitivity of endothelial cells to hemodynamic forces and responsiveness to laminar blood flow.⁷ In agreement with these findings, inhibition of the HEG1–KRIT1 interaction by HKi2 mimics many of the transcriptional effects of laminar blood flow on the endothelium, including increased expression of genes that encode anticoagulants (e.g., *THBD*) and suppressed expression of genes that antagonize angiogenesis (e.g., *THBS1*) and NF κ B-driven proinflammatory genes (e.g., *CCL2*).

In addition, previous studies have shown that mechanotransduction via fluid shear stress^{42–44} and loss of CCM genes^{38,45–47} can mediate Akt activation. Indeed, we found that acute inhibition of the endothelial HEG1–KRIT1 interaction with HKi2 rapidly increases Akt activity, which can be abrogated by inhibition of either Akt or PI3K. However, the molecular connection between flow-induced mechanotransduction and the HEG1–KRIT1 protein complex is still unclear.⁴⁸ Rap1 has been proposed to be activated by laminar shear stress to promote the endothelial mechanosensing protein complex by increasing the association between PECAM1–VEGFR2–VE-cadherin and subsequent Akt signaling.⁴⁹ Importantly, Rap1 activity regulates the junctional localization of KRIT1,⁴ and our previous crystal structure analysis revealed that HEG1–KRIT1–Rap1 can form a ternary complex.³ We showed that there is no competition between HEG1 binding and Rap1 binding to the KRIT1 FERM domain, and we do not expect that HKi2 binding would affect Rap1 binding either. In fact, here we crystallized the KRIT1–Rap1 complex in the presence of HKi's because they diffract better than the KRIT1 FERM alone, supporting that HKi's do not affect Rap1 binding to KRIT1. It is tempting to speculate that inhibition of the endothelial HEG1–KRIT1 protein interaction alters Rap1 activity,⁴ subsequently leading to an increase in Akt activity, although this needs to be further investigated. The HEG1–KRIT1 protein complex may be interconnected to mechanosensing proteins that respond to flow-induced mechanotransduction,^{44,50} a hypothesis that can now be further elucidated with the new small-molecule tools developed through this study to disrupt the HEG1–KRIT1 protein complex.

5 | CONCLUSIONS

In summary, this research utilizes structural insights and a novel high-throughput screening assay to identify a series of hydroxy naphthaldehyde inhibitors of HEG1–KRIT1. These newly identified small-molecule inhibitors are promising pharmacological tools that can be used to investigate the

signaling events that follow disruption of HEG1–KRIT1 protein-protein interaction with previously inaccessible temporal precision. We use one of these inhibitors in ECs in culture and zebrafish to establish the role of HEG1–KRIT1 interaction in the regulation of endothelial cell: i) gene expression of *KLF4* and *KLF2*, and their important transcriptional targets; and ii) Akt activation. These results reveal that the integrity of the HEG1–KRIT1 interaction is intimately linked to transcription factors central to the response of ECs to blood flow. Additionally, acute pharmacological inhibition of the HEG1–KRIT1 interaction, under static conditions, can mimic many of the transcriptional effects of blood flow. Thus, small-molecule inhibitors of the HEG1–KRIT1 protein interaction and their ability to upregulate the transcription factors *KLF2* and *KLF4*, make them highly desirable as research tools, and could also make them valuable as future therapeutic options for mimicking blood flow.

ACKNOWLEDGMENT

The authors thank Mark H. Ginsberg for valuable discussions. This research used resources of the Advanced Light Source, which is a DOE Office of Science User Facility under contract no. DE-AC02-05CH11231. This work was supported by the National Institutes of Health grants K01HL 133530, P01HL151433-01 (to M.A.L.-R.), and NS 092521 (to M.H.G.), the UCSD Academic Senate RS164R-GINGRAS (to A.R.G.), and UC Multi-campus Research Program MRP-17-454909 (to A.R.G. and C.B.). The atomic coordinates and structure factors have been deposited in the Protein Data Bank, www.wwpdb.org (PDB ID code 6OQ4, 6OQ3, and 6UZK). Sequencing data have been deposited in Gene Expression Omnibus (GEO) under accession no. GSE137450.

AUTHOR CONTRIBUTIONS

A.R. Gingras, C. Ballatore, and M.A. Lopez-Ramirez designed research; M.A. Lopez-Ramirez, S. McCurdy, M.K. Haynes, W. Li, B. Gongol, and A.R. Gingras analyzed data; M.A. Lopez-Ramirez, S. McCurdy, M.K. Haynes, P. Hale, C.H.J. Choi, W. Li, K. Francisco, K. Oukoloff, M. Bautista, H. Sun, B. Gongol, and A.R. Gingras performed research; M.A. Lopez-Ramirez, S. McCurdy, C. Ballatore and A.R. Gingras wrote the paper; C. Ballatore contributed to synthesis and design of new inhibitors; B. Gongol and J. Y. Shyy provided expertise in analyzing the RNA-Seq data in the context of flow; and L.A. Sklar provided guidance on assay development, performance, and miniaturization as well as access to the small-molecule libraries, analytical tools, and software necessary to perform and record experiments.

ORCID

Brendan Gongol  <https://orcid.org/0000-0001-9627-613X>
 Alexandre R. Gingras  <https://orcid.org/0000-0002-5373-0176>

REFERENCES

1. Kleaveland B, Zheng X, Liu JJ, et al. Regulation of cardiovascular development and integrity by the heart of glass-cerebral cavernous malformation protein pathway. *Nat Med*. 2009;15:169–176.
2. Gingras AR, Liu JJ, Ginsberg MH. Structural basis of the junctional anchorage of the cerebral cavernous malformations complex. *J Cell Biol*. 2012;199:39–48.
3. Gingras AR, Puzon-McLaughlin W, Ginsberg MH. The structure of the ternary complex of Krev interaction trapped 1 (KRIT1) bound to both the Rap1 GTPase and the heart of glass (HEG1) cytoplasmic tail. *J Biol Chem*. 2013;288:23639–23649.
4. Glading A, Han J, Stockton RA, Ginsberg MH. KRIT-1/CCM1 is a Rap1 effector that regulates endothelial cell cell junctions. *J Cell Biol*. 2007;179:247–254.
5. Gingras AR, Liu JJ, Ginsberg MH. Structural basis of the junctional anchorage of the cerebral cavernous malformations complex. *J Cell Biol*. 2012;199:39–48.
6. Li X, Zhang R, Draheim KM, Liu W, Calderwood DA, Boggon TJ. Structural basis for small G protein effector interaction of Ras-related protein 1 (Rap1) and adaptor protein Krev interaction trapped 1 (KRIT1). *J Biol Chem*. 2012;287:22317–22327.
7. Donat S, Lourenco M, Paolini A, Otten C, Renz M, Abdelilah-Seyfried S. Hg1 and Ccm1/2 proteins control endocardial mechanosensitivity during zebrafish valvulogenesis. *Elife*. 2018;7:e28939.
8. Mably JD, Mohideen MA, Burns CG, Chen JN, Fishman MC. Heart of glass regulates the concentric growth of the heart in zebrafish. *Curr Biol*. 2003;13:2138–2147.
9. Whitehead KJ, Plummer NW, Adams JA, Marchuk DA, Li DY. Ccm1 is required for arterial morphogenesis: implications for the etiology of human cavernous malformations. *Development*. 2004;131:1437–1448.
10. Hogan BM, Bussmann J, Wolburg H, Schulte-Merker S. ccm1 cell autonomously regulates endothelial cellular morphogenesis and vascular tubulogenesis in zebrafish. *Hum Mol Genet*. 2008;17:2424–2432.
11. Mably JD, Chuang LP, Serluca FC, Mohideen MA, Chen JN, Fishman MC. Santa and valentine pattern concentric growth of cardiac myocardium in the zebrafish. *Development*. 2006;133:3139–3146.
12. Cuttano R, Rudini N, Bravi L, et al. KLF4 is a key determinant in the development and progression of cerebral cavernous malformations. *EMBO Mol Med*. 2016;8:6–24.
13. Zhou Z, Rawnsley DR, Goddard LM, et al. The cerebral cavernous malformation pathway controls cardiac development via regulation of endocardial MEKK3 signaling and KLF expression. *Dev Cell*. 2015;32:168–180.
14. Zhou Z, Tang AT, Wong WY, et al. Corrigendum: cerebral cavernous malformations arise from endothelial gain of MEKK3-KLF2/4 signalling. *Nature*. 2016;536:488.
15. Lopez-Ramirez MA, Fonseca G, Zeineddine HA, et al. Thrombospondin1 (TSP1) replacement prevents cerebral cavernous malformations. *J Exp Med*. 2017;214:3331–3346.
16. Renz M, Otten C, Faurobert E, et al. Regulation of beta1 integrin-Klf2-mediated angiogenesis by CCM proteins. *Dev Cell*. 2015;32:181–190.
17. Fisher OS, Deng H, Liu D, et al. Structure and vascular function of MEKK3-cerebral cavernous malformations 2 complex. *Nat Commun*. 2015;6:7937.

18. Chistiakov DA, Orekhov AN, Bobryshev YV. Effects of shear stress on endothelial cells: go with the flow. *Acta Physiol.* 2017;219:382–408.
19. Gore AV, Monzo K, Cha YR, Pan W, Weinstein BM. Vascular development in the zebrafish. *Cold Spring Harb Perspect Med.* 2012;2:a006684.
20. Huddleson JP, Ahmad N, Srinivasan S, Lingrel JB. Induction of KLF2 by fluid shear stress requires a novel promoter element activated by a phosphatidylinositol 3-kinase-dependent chromatin-remodeling pathway. *J Biol Chem.* 2005;280:23371–23379.
21. Parmar KM, Nambudiri V, Dai G, Larman HB, Gimbrone MA Jr, Garcia-Cardena G. Statins exert endothelial atheroprotective effects via the KLF2 transcription factor. *J Biol Chem.* 2005;280:26714–26719.
22. Gingras AR, Puzon-McLaughlin W, Bobkov AA, Ginsberg MH. Structural basis of dimeric rasip1 RA domain recognition of the Ras subfamily of GTP-binding proteins. *Structure.* 2016;24:2152–2162.
23. Tucker J, Sczakiel G, Feuerstein J, John J, Goody RS, Wittinghofer A. Expression of p21 proteins in *Escherichia coli* and stereochemistry of the nucleotide-binding site. *EMBO J.* 1986;5:1351–1358.
24. Edwards BS, Sklar LA. Flow cytometry: impact on early drug discovery. *J Biomol Screen.* 2015;20:689–707.
25. Zhang JH, Chung TD, Oldenburg KR. A simple statistical parameter for use in evaluation and validation of high throughput screening assays. *J Biomol Screen.* 1999;4:67–73.
26. Kabsch W. Xds. *Acta Crystallogr D Biol Crystallogr.* 2010;66:125–132.
27. Collaborative Computational Project, Number 4. The CCP4 suite: programs for protein crystallography. *Acta Crystallogr D Biol Crystallogr.* 1994;50:760–763.
28. de Kreuk BJ, Gingras AR, Knight JD, Liu JJ, Gingras AC, Ginsberg MH. Heart of glass anchors Rasip1 at endothelial cell-cell junctions to support vascular integrity. *Elife.* 2016;5.
29. Lopez-Ramirez MA, Fischer R, Torres-Badillo CC, et al. Role of caspases in cytokine-induced barrier breakdown in human brain endothelial cells. *J Immunol.* 2012;189:3130–3139.
30. Heckel E, Boselli F, Roth S, et al. Oscillatory flow modulates mechanosensitive klf2a expression through trpv4 and trpp2 during heart valve development. *Curr Biol.* 2015;25:1354–1361.
31. Kanda T, Sullivan KF, Wahl GM. Histone-GFP fusion protein enables sensitive analysis of chromosome dynamics in living mammalian cells. *Curr Biol.* 1998;8:377–385.
32. Hopkins AL, Keseru GM, Leeson PD, Rees DC, Reynolds CH. The role of ligand efficiency metrics in drug discovery. *Nat Rev Drug Discovery.* 2014;13:105–121.
33. Johnson TW, Gallego RA, Edwards MP. Lipophilic efficiency as an important metric in drug design. *J Med Chem.* 2018;61:6401–6420.
34. Weksler B, Romero IA, Couraud PO. The hCMEC/D3 cell line as a model of the human blood brain barrier. *Fluids and barriers of the CNS.* 2013;10:16.
35. Gore AV, Lampugnani MG, Dye L, Dejana E, Weinstein BM. Combinatorial interaction between CCM pathway genes precipitates hemorrhagic stroke. *Dis Model Mech.* 2008;1:275–281.
36. Sako K, Fukuhara S, Minami T, et al. Angiopoietin-1 induces Kruppel-like factor 2 expression through a phosphoinositide 3-kinase/AKT-dependent activation of myocyte enhancer factor 2. *J Biol Chem.* 2009;284:5592–5601.
37. Nayak L, Lin Z, Jain MK. "Go with the flow": how Kruppel-like factor 2 regulates the vasoprotective effects of shear stress. *Antioxid Redox Signal.* 2011;15:1449–1461.
38. Kar S, Samii A, Bertalanffy H. PTEN/PI3K/Akt/VEGF signaling and the cross talk to KRIT1, CCM2, and PDCD10 proteins in cerebral cavernous malformations. *Neurosurg Rev.* 2015;38:229–237.
39. Kozakov D, Hall DR, Jehle S, et al. Ligand deconstruction: why some fragment binding positions are conserved and others are not. *Proc Natl Acad Sci U S A.* 2015;112:E2585–E2594.
40. Park J, Fu H, Pei D. Peptidyl aldehydes as reversible covalent inhibitors of SRC homology 2 domains. *Biochemistry.* 2003;42:5159–5167.
41. Cullere X, Plovie E, Bennett PM, MacRae CA, Mayadas TN. The cerebral cavernous malformation proteins CCM2L and CCM2 prevent the activation of the MAP kinase MEKK3. *Proc Natl Acad Sci U S A.* 2015;112:14284–14289.
42. Jin ZG, Ueba H, Tanimoto T, Lungu AO, Frame MD, Berk BC. Ligand-independent activation of vascular endothelial growth factor receptor 2 by fluid shear stress regulates activation of endothelial nitric oxide synthase. *Circ Res.* 2003;93:354–363.
43. Jin ZG, Wong C, Wu J, Berk BC. Flow shear stress stimulates Gab1 tyrosine phosphorylation to mediate protein kinase B and endothelial nitric-oxide synthase activation in endothelial cells. *J Biol Chem.* 2005;280:12305–12309.
44. Coon BG, Baeyens N, Han J, et al. Intramembrane binding of VE-cadherin to VEGFR2 and VEGFR3 assembles the endothelial mechanosensory complex. *J Cell Biol.* 2015;208:975–986.
45. Zhu Y, Wu Q, Xu JF, et al. Differential angiogenesis function of CCM2 and CCM3 in cerebral cavernous malformations. *Neurosurg Focus.* 2010;29:E1.
46. He Y, Zhang H, Yu L, et al. Stabilization of VEGFR2 signaling by cerebral cavernous malformation 3 is critical for vascular development. *Science signaling.* 2010;3:ra26.
47. Louvi A, Chen L, Two AM, Zhang H, Min W, Gunel M. Loss of cerebral cavernous malformation 3 (Ccm3) in neuroglia leads to CCM and vascular pathology. *Proc Natl Acad Sci USA.* 2011;108:3737–3742.
48. Baeyens N, Bandyopadhyay C, Coon BG, Yun S, Schwartz MA. Endothelial fluid shear stress sensing in vascular health and disease. *J Clin Invest.* 2016;126:821–828.
49. Lakshmikanthan S, Zheng X, Nishijima Y, et al. Rap1 promotes endothelial mechanosensing complex formation, NO release and normal endothelial function. *EMBO Rep.* 2015;16:628–637.
50. Stefanini L, Bergmeier W. RAP GTPases and platelet integrin signaling. *Platelets.* 2018;30:41–47.

SUPPORTING INFORMATION

Additional supporting information may be found online in the Supporting Information section.

How to cite this article: Lopez-Ramirez MA, McCurdy S, Li W, et al. Inhibition of the HEG1–KRIT1 interaction increases KLF4 and KLF2 expression in endothelial cells. *FASEB BioAdvances.* 2021;3:334–355. <https://doi.org/10.1096/fba.2020-00141>